Acta Pharmaceutica Sinica B 2026;16(7):4592−4615

Chinese Pharmaceutical Association
Institute of Materia Medica, Chinese Academy of Medical Sciences

Acta Pharmaceutica Sinica B

www.elsevier.com/locate/apsb
www.sciencedirect.com

ORIGINAL ARTICLE

Photobiomodulation-reprogrammed extracellular vesicles delivered *via* a biodegradable microneedle patch promote cardiac repair by enhancing glycolytic metabolism

Yining Liu[a,b,†], Sijia Li[a,b,†], Ao Cai[a,b,†], Wei Li[a,b,†], Wanyu Zhang[a,b], Tianlong Li[d], Manjie Zhang[a,b], Chenlu Liu[d], Wenya Ma[a,b], Yuqing Lin[a,b], Hanjing Li[a,b], Xinlu Gao[a,b], Zhongyu Ren[a,b], Hang Yu[a,b], Haoyu Ji[a,b], Xiuxiu Wang[a,b], Yang Yu[a,b], Xu Liu[c], Yifu Shen[c], Ye Tian[e], Faqian Li[f], Yu Liu[c], Zhenwei Pan[b,*], Baofeng Yang[b,g,*], Benzhi Cai[a,b,g,*]

[a]*Department of Pharmacy at the Second Affiliated Hospital, Harbin Medical University, Harbin 150086, China*
[b]*State Key Laboratory of Frigid Zone Cardiovascular Diseases (SKLFZCD), Department of Pharmacology (The State-Province Key Laboratories of Biomedicine Pharmaceutics of China, Key Laboratory of Cardiovascular Research, Ministry of Education), College of Pharmacy, Harbin Medical University, Harbin 150081, China*
[c]*Department of Laboratory Medicine at the Fourth Affiliated Hospital, Harbin Medical University, Harbin 150001, China*
[d]*School of Mechanical and Electrical Engineering, Harbin Institute of Technology, Harbin 150006, China*
[e]*Department of Pathophysiology, Key Laboratory of Cardiovascular Physiology, Harbin Medical University, Harbin 150081, China*
[f]*Department of Pathology & Laboratory Medicine, Joe R. and Teresa Lozano Long School of Medicine, University of Texas Health Science Center at San Antonio, San Antonio, TX 78229, USA*
[g]*Institute of Clinical Pharmacy, NHC Key Laboratory of Cell Transplantation, The Heilongjiang Key Laboratory of Drug Research, Harbin Medical University, Harbin 150081, China*

Received 24 November 2025; received in revised form 10 February 2026; accepted 3 March 2026

*Corresponding authors.
E-mail addresses: panzw@ems.hrbmu.edu.cn (Zhenwei Pan), yangbf@ems.hrbmu.edu.cn (Baofeng Yang), caibz@ems.hrbmu.edu.cn (Benzhi Cai).
[†]These authors made equal contributions to this work.
Peer review under the responsibility of Chinese Pharmaceutical Association and Institute of Materia Medica, Chinese Academy of Medical Sciences.

https://doi.org/10.1016/j.apsb.2026.04.015

KEY WORDS

Myocardial infarction;
Cardiac repair;
Stem cell;
Extracellular vesicle;
Photobiomodulation;
Glycolysis metabolism;
Microneedle patch;
MicroRNA

Abstract Stem cell-derived extracellular vehicles (EVs) hold great therapeutic potential for myocardial infarction (MI). However, the efficient production of EVs with high bioactivity remains a critical bottleneck limiting their clinical translation. Here, we demonstrate that conditioned photobiomodulation (PBM) with green light is capable of activating human embryonic stem cells (hESCs) to secrete more EVs with superior cardioprotective activity. These PBM-reprogrammed hESC-EVs improve cardiac recovery in a murine MI model by promoting cardiomyocyte proliferation and angiogenesis while inhibiting apoptosis. Notably, we validate that these EVs similarly enhance the survival and proliferation of human cardiomyocytes, underscoring their translational potential. Further analysis reveals that this benefit is due to the higher miR-423-3p content in reprogrammed hESC-EVs, which enhances glycolytic metabolism and restores mitochondrial function by regulating the ZBTB7A/PKM2 axis. Moreover, we synthesize a methacryloyl hydrogel microneedle patch with superior biocompatibility, biodegradability, and mechanical strength for loading hESC-EVs, and convey the patch to the infarcted heart *via* a modified delivery apparatus. This system ensures the precise and sustained delivery of EVs to ischemic myocardium, offering a potent treatment for MI. Collectively, this optical and biomaterials-based approach efficiently prepares EVs with higher cardioprotective activity, providing new therapeutic strategies for heart disease.

1. Introduction

Myocardial infarction (MI) is the leading cause of morbidity and mortality worldwide, posing a serious threat to patients' health and quality of life[1]. During the pathological process of MI, massive functional cardiomyocytes (CMs) undergo necrosis and apoptosis due to persistent ischemia and hypoxia injury. The missing CMs are then substituted by fibrous scar tissue, resulting in ventricular remodeling, decreased heart function, and ultimately heart failure[2,3]. Although significant advances have been made in surgical, interventional, and pharmacological treatments, they fail to compensate for CMs loss following MI[4]. For decades, stem cell-based regenerative medicine has shed light on MI treatment. The transplanted stem cells improve cardiac function by promoting myocardial contraction and angiogenesis through inotropic coupling and paracrine secretion[5]. Embryonic stem cells (ESCs), a type of pluripotent cell derived from the inner cells of human blastocysts, have been explored in cell therapies for a range of diseases, including age-related macular degeneration, spinal cord injury, and type 1 diabetes[6]. Notably, ESCs also hold great promise for cardiac repair due to their self-renewal and differentiation capacities. However, their clinical application is constrained by some challenges, including significant risk of immune rejection and tumorigenicity, undesirable biodistribution and engraftment, and ethical issues[7,8].

Extracellular vesicles (EVs), tiny membrane vesicles with lipid bilayers that carry proteins, mRNA, non-coding RNA, and lipids, are important mediators for intercellular information transmission and material exchange[9,10]. EVs derived from stem cells have demonstrated considerable therapeutic properties with fewer safety concerns and "off-the-shelf" convenience[11,12]. A recent study indicated that EVs secreted by embryonic stem cells (ESC-EVs) effectively ameliorated age-related pathological phenotypes and rescued the transcriptome profile in aged mice[13]. Additionally, ESC-EVs have been shown to possess certain anti-tumor properties[14]. In a study by Khan et al.[15], mouse ESC-EVs were found to enhance neovascularization and CM survival while reducing fibrosis, thereby improving cardiac function following MI. Therefore, the EV-based "cell-free" therapeutic strategy with the advantages of superior biocompatibility might be an ideal alternative to ESCs in clinical treatment. Nevertheless, EV therapy for heart repair is generally constrained by several challenges, including low yield, short half-life, and poor tissue retention. To achieve therapeutic efficacy, repeated dosing is needed, whereas multi-dose intracardiac injection of EVs is highly invasive and time-consuming for surgery[16-18]. Consequently, numerous studies have begun to focus on promoting the therapeutic effects of stem cell-derived EVs through various conditions[19].

Photobiomodulation (PBM) is a non-invasive therapy that utilizes low-intensity, biocompatible light within specific wavelengths to penetrate tissue and interact with intracellular chromophores. This interaction triggers a series of photophysical and photochemical events that ultimately regulate the fate of various cells and tissues[20]. Studies have shown that PBM can induce multiple positive biological responses, including enhancing cell proliferation, promoting metabolic processes, and alleviating inflammatory responses[21-23]. Consequently, this technology has gained widespread clinical adoption for promoting wound healing, alleviating pain, and facilitating the regeneration of muscle and nerve tissue[21,24]. Notably, the application of PBM, delivered *via* lasers or light-emitting diodes (LEDs), is also recognized as a potent tool for effectively regulating the biological characteristics and functions of stem cells, independent of genetic or pharmaceutical interventions[25,26]. However, the current research primarily focuses on the direct intracellular effects of PBM on stem cells. Whether PBM influences the secretory function of ESCs, thereby altering the composition and biological function of the EVs derived from them, remains unexplored. Furthermore, in addition to regulating the biological activity of EVs, the application of advanced delivery systems to enhance the retention and enable sustained release of EVs at the injury site is equally critical. In recent years, the microneedle (MN) patch has emerged as a promising long-term local drug delivery platform in regenerative medicine. They offer minimally invasive access, spatiotemporal control over drug release, and improved local retention, which have been successfully applied in the repair of diabetic and chronic refractory wounds[27-29]. Encouraged by these advances, we believe that adapting this functional platform for cardiac delivery could overcome the limitations of direct EV injection for myocardial repair.

In this study, we developed a protocol to treat human embryonic stem cells (hESCs) with PBM and subsequently isolated the released EVs. Our results suggested that PBM with 520 nm wavelength irradiation (green light) could stimulate hESCs to produce EVs with enhanced bioactivity. These EVs modulated glycolytic metabolism and mitochondrial homeostasis, thereby promoting CM cell cycle reentry, inhibiting CM apoptosis, and facilitating angiogenesis, which markedly restored cardiac function post-MI. Furthermore, to address the issue of low tissue retention after local intramyocardial injection of EVs, we prepared a gelatin methacryloyl (GelMA) MN patch with superior biocompatibility, biodegradability, and mechanical strength for loading hESC-EVs and then attached the patch to the infarcted heart *via* a modified apparatus. GelMA MN patch enhanced the therapeutic efficacy of hESC-EVs on MI by enabling their targeted and sustained release. Collectively, our findings demonstrate that this optical and biomaterials-based approach can effectively prepare EVs with enhanced cardioprotective activity for the treatment of ischemic heart diseases.

2. Materials and methods

2.1. Study design

The sample sizes were determined based on similar publications in the field. Animal randomization was performed using a random number generator (www.randomizer.org). All experiments and data analyses were conducted in a blinded manner. Specifically, for *in vivo* assessments such as echocardiography, both the operator and the data analyst were blinded to group allocation. For *in vitro* experiments, culture wells were randomly assigned to treatment groups using a random number generator (Microsoft Excel).

2.2. Ethics statement

All experimental protocols involving human embryonic stem cells (hESCs) and animals in this study were reviewed and approved by the Institutional Animal Care and Use Committee of Harbin Medical University (Approval No. IRB3085724). The whole experimental process was carried out according to the approved procedures and adhered to the ARRIVE reporting guidelines 2.0. Healthy male C57BL/6J mice were purchased from Liaoning Changsheng Biotechnology Co., Ltd. The hESC line (cell code: CB0003) was obtained from the National Stem Cell Resource Center of China (Beijing, China). According to the certificate provided by the resource center (Lot No.: 2023-06-01), this cell line was derived from the inner cell mass of a normal 5−7-day blastocyst. The derivation process was conducted in full compliance with the Chinese regulations on human genetic resources, with ethical approval from the collaborating hospital and written informed consent obtained from the donor. This study strictly complied with the Ethical Guidelines for Human Embryonic Stem Cell Research in China, without any unethical experimental operations.

2.3. Animal studies

To avoid the influence of estrogen fluctuations in females, male C57BL/6J mice (6−8 weeks old) were used in this study to ensure consistent results[30]. All mice were maintained in a temperature-controlled facility with a 12 h light/dark cycle at 22.5 ± 1 °C and 50 ± 5% humidity. The procedure for the MI model was conducted as previously reported[31]. In brief, mice were anesthetized in the gas chamber with 2%−4% isoflurane (Midmark Corporation, Versailles, OH, USA) and ventilated *via* orotracheal intubation. The coronary artery of left anterior descending (LAD) was ligated with a 7-0 prolene suture until the myocardium was locally pale. To standardize the infarct model, echocardiography was performed 4 h post-MI for inclusion and randomization. MI mice with left ventricular ejection fraction (LVEF) between 30% and 45% were included. Subsequently, eligible mice were randomly assigned to experimental groups using a stratified randomization procedure based on their LVEF values, ensuring that the baseline injury was consistent across all groups ($P > 0.05$). A separate Sham group underwent identical surgical procedures except for LAD ligation. All procedures were performed by the same experienced operator to minimize variability. Following randomization, mice received intramyocardial injections into the border zone of the infarcted heart at three sites using a 31 G needle. The treatment groups received either CEE (control hESC-EVs) or PbEE (PBM-reprogrammed hESC-EVs) at a dose of 3×10^{10} particles in 30 μL saline, while the MI control group received an equal volume of saline. In addition, MN patches loaded with 3×10^{10} EV particles were attached to the infarct area of mice.

Recombinant adeno-associated virus serotype 9 (AAV9) vectors harboring the cardiac troponin T (cTnT) promoter to drive *Zbtb7a* expression (AAV9-cTNT-ZBTB7A) were constructed and supplied by GenePharma Co., Ltd., (Shanghai, China). The backbone vector AAV9-cTNT without the *Zbtb7a* gene was employed as the negative control (AAV9-NC). Mice received tail-vein injection of AAV9-cTNT-ZBTB7A or AAV9-NC at a dosage of 1.5×10^{11} viral genomes (vg) per mouse. One week following AAV9 administration, all mice were subjected to MI surgery. Subsequently, PbEE (3×10^{10} particles dissolved in 30 μL normal saline) was injected into the infarct border zone *via* intramyocardial injection.

2.4. Culture and photostimulation of hESCs

The hESCs were routinely cultured in PSCeasy II Human pluripotent stem cell culture medium (CA1014500, Cellapy, Beijing, China) on plates coated with Matrix (PSCeasy Human pluripotent stem cell coating working solution, CA3003100, Cellapy, Beijing, China) under the condition of 37 °C with 5% CO_2. The cells were passaged with 0.5 mmol/L DissoEasy Human pluripotent stem cell digestion solution (CA1023100, Cellapy, Beijing, China) every 3 days and replaced with fresh medium daily. Prior to irradiation, 2 mL of complete medium was added to each well of the 6-well plate. hESCs were irradiated with an LED array emitting 500−540 nm light (peak at 520 nm) with a uniform beam profile. The applied power density was 2.5 mW/cm^2 for 30 min per session, corresponding to an energy density of 4.5 J/cm^2. The LED array was perpendicularly positioned 11.5 cm above the uncovered plate to avoid light scattering, with irradiation covering the entire well area. To validate the spatial uniformity of irradiation across the culture area, the irradiance profile was characterized using a calibrated optical power meter (p0023164, Thorlabs, NJ, USA). We performed irradiance mapping at 30 predefined points on the six-well plate, comprising five points per well (the center and four edge points). The average irradiance across the target area was 2.50 ± 0.19 mW/cm^2 (mean ± SD). The coefficient of variation across all measured points was 5.82%, demonstrating a uniform irradiance profile. Throughout irradiation, the temperature was

maintained at 37 °C. The control group underwent identical conditions with the light source off. Following this treatment, all cells (both irradiated and control) were cultured for an additional 48 h under standard conditions, and the EVs in the supernatant were collected for subsequent experiments. The specifications of the light source are detailed in Table 1.

2.5. TRP inhibition

For transient receptor potential (TRP) channel inhibition experiments, hESCs were pre-treated with 5 μmol/L SKF-96365 (130495-35-1, MCE, NJ, USA), a widely used TRP channel blocker. The inhibitor was added to the cell culture medium 10 min prior to green light stimulation and remained present throughout the entire light stimulation period to ensure sustained TRP channel inhibition. Control groups were treated with an equivalent volume of vehicle solution under identical culture conditions to exclude non-specific effects.

2.6. Isolation and characterization of hESC-EVs

EVs secreted from hESCs in the supernatant were isolated by ultracentrifugation. The specific steps are as follows: the medium of hESCs was first centrifuged for 20 min at 3000×*g* to remove dead cells. The supernatant was centrifuged for 30 min at 10,000×*g* to remove cellular debris and then filtered through a 0.22 μm microporous filter membrane. Finally, EVs were obtained by centrifuging the supernatant at 100,000×*g* for 70 min and dissolved in PBS. Subsequently, nanoparticle tracking analysis (NTA) was performed to analyze the size and particle concentration of EVs. The microstructure of EVs was characterized by transmission electron microscopy (TEM; Hitachi HT7800, Tokyo, Japan). Western blot was used to detect the expression of EV markers, including CD63 (ab134045, Abcam, Cambridge, UK, 1:500), TSG101 (ab125011, Abcam, Cambridge, UK, 1:500), and Flotillin-1 (ab133497, Abcam, Cambridge, UK, 1:10000).

2.7. Tracer labeling of EVs

EVs were labeled using the EV WisTracker Kit (WSR0001, WisDelivery Biotechnology, Wuhan, China) following the manufacturer's protocol. Briefly, EVs were incubated with WisTracker 500X (1:500, *v*/*v*) at room temperature for 30 min protected from light, with gentle mixing to ensure homogenous dispersion. To neutralize excess dye, WisTracker Remover (1:100, *v*/*v*) was added to the solution, which was then incubated in the dark for 10 min. Labeled EVs were subsequently purified by ultracentrifugation at 100,000×*g* for 70 min to remove free dye. For internalization assays, primary neonatal mouse cardiomyocytes (NMCMs) and human umbilical vein endothelial cells (HUVECs) were incubated with the labeled EVs for 12 and 6 h, respectively. EV uptake was then evaluated using immunofluorescence microscopy (Leica Microsystems, Wetzlar, Germany).

Lentiviral vectors expressing CD63-GFP (LV6-EF1a-CD63-GFP) were obtained from GenePharma Co., Ltd., (Shanghai, China). The hESCs were infected with LV6-EF1a-CD63-GFP (50 MOI) for 48 h, and then EVs were isolated from the conditioned medium by ultracentrifugation. To evaluate EV uptake, NMCMs were incubated with the CD63-GFP-labeled EVs for 12 h. Internalization was subsequently visualized using a fluorescence microscope (Leica Microsystems, Wetzlar, Germany).

2.8. Culture and treatment of NMCMs

NMCMs were isolated from the hearts of 1- to 3-day-old C57BL/6J mice as previously described[32]. In brief, small pieces of heart tissue were completely digested with 0.25% trypsin (T1300, Solarbio, Beijing, China), and the mixture was centrifuged at 1000 rpm (SC-3610, ZONKIA, Anhui, China) for 5 min. The resuspended cells were cultured in DMEM (12491015, Life Technologies, Carlsbad, CA, USA) with 10% fetal bovine serum (A5256701, Gibco, Carlsbad, CA, USA) and 1% penicillin and streptomycin (A5873601, Life Technologies, Carlsbad, USA) for 2 h. The non-adherent cardiomyocytes were then transferred to a new plate and cultured in DMEM with 10% fetal bovine serum, 1% penicillin and streptomycin under normoxic conditions (atmospheric 21% O_2) at 37 °C for 48 h. Upon reaching approximately 80% confluence (1×10^6cells in 2 mL medium), NMCMs were treated with CEE or PbEE at a final concentration of 3×10^9 particles/mL. To induce hypoxia, NMCMs were placed in a tri-gas incubator (Thermo Fisher, Waltham, MA, USA) at 1% O_2, 5% CO_2, 94% N_2 for 24 h. Subsequently, the cells were harvested to assess apoptosis using the TdT-mediated dUTP nick-end labeling (TUNEL) assay.

Table 1 Parameters of green light irradiation.

Parameter	Value/description
Light source type	LED array
Wavelength (nm)	500−540, peak at 520
Beam profile	Uniform
Power density (mW/cm^2)	2.5
Irradiation mode	Continuous wave
Irradiation time per session (min)	30
Energy density (J/cm^2)	4.5
Distance from source to sample (cm)	11.5
Area of irradiation	Cover the entire area of the 6-well plate
Treatment schedule	Once
Irradiation angle	Perpendicular irradiation to the cell plate
Control group treatment	Same device placement with light source off
Temperature control	Maintained at 37 °C
Culture medium volume (per well)	2 mL complete medium

2.9. Transfection

The miR-423-3p agomir (ago-miR-423-3p), antagomir (antago-miR-423-3p), and their respective negative controls (ago-NC and anta-NC), as well as small interfering RNAs (siRNAs) targeting *Pkm2* (si-PKM2) and *Creb* (si-CREB), were synthesized by GenePharma Co., Ltd. (Shanghai, China). The mouse *Zbtb7a* overexpression plasmid (pcDNA3.1-musZBTB7A-3xFlag; Cat. No. HG-MO010731) was purchased from HonorGene (Changsha, China). Cells were transfected with plasmids using Lipofectamine 2000 (11668019, Invitrogen, Carlsbad, CA, USA), and transfected with siRNAs using RNAiMAX reagent (13778150, Invitrogen, Carlsbad, CA, USA) according to the manufacturer's instructions. The sequence of ago-miR-423-3p is AGCUCGGUCU GAGGCCCCUCAGU, UGAGGGGCCUCAGACCGAGCUUU; antago-miR-423-3p is ACUGAGGGGCCUCAGACCGAGCU; si-PKM2 is GCAAGAACAUCAAGAUCAUTT, AUGAUCUU GAUGUUCUUGCTT; si-CREB is GCCUGCAAACAUU AACCAUTT; AUGGUUAAUGUUUGCAGGCTT.

2.10. Vascular tube formation of HUVECs

The tube formation assay was performed to evaluate the angiogenic potential of HUVECs. Briefly, 24-well plates were coated with Matrigel Basement Membrane Matrix (356234, Corning, NY, USA) and incubated at 37 °C for 30 min to allow polymerization. HUVECs were then seeded onto the solidified Matrigel and incubated with CEE or PbEE at a final concentration of 3×10^9 particles/mL. After 6 h, tube formation was visualized using a light microscope (CKX41, Olympus Corporation, Tokyo, Japan). Images from nine randomly selected fields per well were captured, and the number of vascular tubes was quantified using ImageJ (Version 1.5.3).

2.11. Wound healing assay in vitro

HUVECs were seeded in a 6-well plate and cultured to approximately 90% confluence. A linear wound was created in the cell monolayer using a sterile 200 μL pipette tip. After washing with PBS to remove cell debris, the cells were incubated with CEE or PbEE at a concentration of 3×10^9 particles/mL for 24 h. Images of the wound area were captured at 0 and 24 h using a light microscope (CKX41, Olympus Corporation, Tokyo, Japan). Migration rate was calculated according to Eq. (1):

$$\text{Migration rate } (\%) = (A_0 - A_f)/A_0 \times 100 \quad (1)$$

A_0 represents the initial wound area at 0 h, and A_f represents the remaining wound area at 24 h.

2.12. Fabrication and characterization of EVs-loaded MNs

Gelatin methacryloyl (GelMA; P202405, Curegel Co., Ltd., Wenzhou, China) was dissolved in sterile PBS to prepare 15% (*w*/*v*) precursor solution containing 0.25% (*w*/*v*) lithium phenyl-2,4,6-trimethylbenzoylphosphinate (HY-44076, MCE, NJ, USA) as a photoinitiator. EVs were gently mixed into the GelMA precursor on ice. The mixture was cast into PDMS MN molds, degassed under vacuum, and photocrosslinked with 405 nm light. Subsequently, GelMA solution without EVs was added as a backing layer and further photocrosslinked for 60 s. The MNs were gently demolded and stored at 4 °C in a sealed container before use. The final patch consisted of a circular array (0.6 cm in diameter) of 68 conical needles, with each needle measuring 650 μm in height and 320 μm in base diameter. The morphology of MNs was characterized using scanning electron microscopy (SEM; TESCAN MIRA3, TESCAN, Brno, Czech Republic). Mechanical compression testing for MNs was performed by an electronic mechanical tester (INSTRON 5982, Instron, Norwood, MA, USA). Specifically, the MNs were fixed to a steel plate, and the pressure sensor was approached and pressed against the MN patches at a speed of 5 mm/min.

2.13. The release profile of EVs-loaded MNs in vitro

The cumulative release of EV particles from the MNs was quantified by NTA using a ZetaView Particle Metrix (Particle Metrix GmbH, Inning am Ammersee, Germany). EV-loaded MNs were incubated in release buffer (PBS, pH 7.4) at 37 °C under gentle agitation. At different time points (Day 1 to Day 14), the supernatant was collected for analysis and replaced with fresh buffer. The percentage of release was calculated based on the released particle number relative to the initial loaded amount.

2.14. Construction of microneedle attachment device

Since the mouse heart beats at 600−700 beats/min, it is difficult to immobilize the MNs on the mouse heart using finger pressure. Therefore, we prepared a MN delivery apparatus made of polylactic acid by 3D printing, which works similarly to off-pump coronary aortic bypass grafting stabilizers in clinical settings. The apparatus consists of a working-end and a connecting-end cylinder with diameters of 0.65 and 0.8 cm, respectively. The working end was equipped with a 0.1 cm-diameter penetration hole at the center, and the top was sunk 0.12 cm to form a platform for adsorption and fixation of MNs. The bottom of the connecting end was attached to a suction pipe connected to a negative-pressure device. The difference between the inner and outer diameters ensured the patency of the chamber. When suction was supplied (−8 kPa), myocardial tissues from the infarcted area entered the pump head, allowing the MNs to be passively and completely inserted into the myocardium. Upon cessation of suction supply, the MNs were separated from the pump head.

2.15. Release of EVs-loaded MNs in vivo

To evaluate the retention capability of MNs, PbEE were labeled with the WisTracker probe and encapsulated into the MN patches. The PbEE-loaded MNs were implanted onto the border zone of the infarcted myocardium. As a control, an equivalent amount of labeled PbEE was administered *via* intramyocardial injection. The hearts of mice were collected at Days 0, 3, and 14 post-treatments. The fluorescence intensity of the retained EVs was visualized and quantified using an IVIS imaging system (Xenogen, Cranberry Township, PA, USA).

2.16. Echocardiography

Cardiac function was evaluated 28 days post-MI using a Vevo 1100 system (VisualSonics, Toronto, ON, Canada). Mice were anesthetized and placed on a heated platform to maintain body temperature. M-mode images were acquired from the parasternal short-axis view at the level of the papillary muscles. Left ventricular internal diameters at end-diastole (LVIDd) and at end-

systole (LVIDs) were measured. Subsequently, left ventricular ejection fraction (LVEF) and fractional shortening (LVFS) were calculated using the Vevo LAB software. All measurements were averaged from at least three consecutive cardiac cycles.

2.17. Histological examination

MI mouse hearts were harvested, fixed in 4% paraformaldehyde (P1110, Solarbio, Beijing, China) overnight, and subsequently dehydrated and embedded in paraffin. Serial sections (5 μm thick) were prepared for histological examination. To evaluate structural integrity and potential tissue damage following MN application, sections were stained with Hematoxylin and Eosin (H&E; G1120, Solarbio, Beijing, China). To assess the extent of myocardial fibrosis, hearts collected at Day 28 post-MI were stained with Masson's trichrome (G1340, Solarbio, Beijing, China) according to the manufacturer's protocol. The fibrotic area (stained blue) was quantified using Image-Pro Plus software and expressed as a percentage of the total left ventricular area.

2.18. Immunofluorescence staining

NMCMs, HUVECs, or heart sections were fixed with 4% paraformaldehyde for 20 min and then permeabilized with 0.4% Triton X-100 (P0096, Beyotime, Shanghai, China) for 15 min at room temperature. After washing with PBS, the samples were blocked with goat serum (AR0009, BOSTER, Wuhan, China) for 30 min at 37 °C to minimize nonspecific binding. Next, these samples were co-incubated with primary antibodies against phospho-Histone H3 (ab32107, Abcam, Cambridge, UK, 1:500), Ki67 (ab15580, Abcam, Cambridge, UK, 1:400), Aurora B (ab2254, Abcam, Cambridge, UK, 1:400), Alpha Actinin (GTX29465, Gene Tex, San Antonio, USA, 1:400), and CD31 (ab28364, Abcam, Cambridge, UK, 1:400) at 4 °C overnight, followed by incubation with secondary antibody for 1 h at 37 °C in darkness. Nuclei were stained with DAPI (C0065, Solarbio, Beijing, China, 1:30) for 10 min, and immunofluorescence images were captured with a confocal laser scanning microscope (Leica Microsystems, Wetzlar, Germany).

The positive rate of CMs in heart sections is calculated as follows: 3 heart sections (each section interval 600 μm) from the infarct border zone of each mouse were selected for immunofluorescence staining (the same position was selected in the Sham group and the MI group). Then, images of 5 fields per section were obtained by confocal microscopy. The positive rate of CMs in the above 15 images was manually counted and quantified, and the calculated mean was regarded as the positive rate of each mouse. The detailed statistical methods for the percentage of EdU-, Ki67-, pH3-, or TUNEL-positive CMs in each field are as follows: Cells co-located by Alpha Actinin (green) and DAPI (blue) were identified as CMs (total number of CMs). Cells co-located by Alpha Actinin (green), DAPI (blue), and EdU, Ki67, pH3, or TUNEL (red) were regarded as proliferative or apoptotic CMs. Positive rate was calculated according to Eq. (2):

$$\text{Positive rate } (\%) = (\text{Number of proliferative or apoptotic CMs/Number of total CMs}) \times 100 \quad (2)$$

2.19. Wheat germ agglutinin (WGA) staining

The heart sections were incubated with WGA (W849, Invitrogen, Carlsbad, USA) for 30 min at 37 °C to identify cell borders, followed by staining with DAPI for 10 min to detect nuclei. WGA-stained cells were visualized using a fluorescent microscope (Leica Microsystems, Wetzlar, Germany). Then, the CM surface area was manually traced and quantified using ImageJ (Version 1.5.3).

2.20. Dissociation of CMs from adult MI mice using the Langendorff-perfusion method

Adult CMs from adult C57BL/6J mice were isolated using a Langendorff perfusion system as previously described[33]. In brief, the aortic arch was connected to the needle of a syringe and perfused with Tyrode solution (in mmol/L: NaCl 150; KCl 5.4; HEPES 5; $MgCl_26H_2O$ 1.2; NaH_2PO_4 2; Glucose 10; pH adjusted to 7.36−7.40 with NaOH). The enzyme-containing solution, containing 1 mg/mL type II collagenase (17101015, Invitrogen, Carlsbad, CA, USA) and 0.75 mg/mL bovine serum albumin V (SA8130, Solarbio, Beijing, China), was then added to the Langendorff perfusion system to digest the hearts at 37 °C. When the tissue turned soft, the heart was cut off and gently blown in Tyrode's solution containing 200 μmol/L $CaCl_2$ and 4% bovine serum albumin V, and the CMs were left to settle at room temperature. The isolated CMs were fixed with 4% paraformaldehyde for 20 min at room temperature, and stained with Alpha Actinin and DAPI, respectively. CMs were classified as mononucleated (1N), binucleated (2N), or multinucleated (>2N) based on nuclear count. The percentage of each population was calculated from at least three independent fields per heart using a Leica fluorescence microscope.

2.21. Seahorse analyses

NMCMs were inoculated into Seahorse XFe24 cell culture plates (102342-100, Agilent Technologies, USA) and transfected with NC, ago-miR-423-3p, and ago-miR-423-3p + OE-ZBTB7A, respectively. 48 h after transfection, the glycolysis of CMs was examined by measuring the extracellular acidification rate (ECAR) using the Seahorse XF Glycolysis Stress Test Kit (103020-100, Agilent Technologies, USA), and the Agilent Hippocampus XFe24 Cellular Energy Metabolism Assay System (Agilent Technologies, Santa Clara, CA, USA) according to the manufacturer's instructions.

2.22. Cardiac differentiation from hESCs

Cardiac differentiation was induced from hESCs (H9 cell line) as described in a previous report[34]. Briefly, at the onset of differentiation, hESCs were cultured in RPMI 1640 medium supplemented with B27 minus insulin (A1895601, Thermo Fisher Scientific, Waltham, MA, USA). On Days 0−1, 6 μmol/L CHIR (HY-10182, MCE, NJ, USA) was added to the medium. On Days 3−5, 2 μmol/L wnt-C59 (HY-15659, MCE, NJ, USA) was added to the medium. On Day 7 of differentiation, the medium was replaced with RPMI 1640 plus B27 supplement (17504044, Thermo Fisher, Waltham, USA), and the medium was changed every 48 h until pulsing cardiomyocytes derived from hESCs (hESC-CMs) were observed. For functional assays, hESC-CMs were treated with CEE, PbEE, or PbEE-loaded microneedle patches (PbEE@MN) at a concentration of 3×10^9 particles/mL. After 3 days of hypoxia treatment, the apoptosis of hESC-CMs was detected by TUNEL assay (A113-03, Vazyme, Nanjing, China). After 7 days of co-incubation (without hypoxia), the

expressions of Ki67 and pH3 in hESC-CMs were detected by immunofluorescence.

2.23. Western blot analysis

Proteins were extracted from cells and EVs using RIPA lysis buffer (P0013B, Beyotime, Shanghai, China), and protein concentrations were determined by BCA Protein Assay kit (P0010, Beyotime, Shanghai, China). An equal amount of 60 μg protein from each group was fractionated by 10% or 12.5% SDS-PAGE and electroblotted onto a nitrocellulose membrane (Pall, Port Washington, NY, USA). After blocking in 5% milk for 1.5 h, the membranes were incubated with primary antibody overnight at 4 °C, including ZBTB7A (RM6296, Suzhou, China, 1:1000), PKM2 (R321004, Zen-Bio, Chengdu, China, 1:500), Bcl2 (CY6717, Abways Technology, Shanghai, China, 1:500), Bax (CY5059, Shanghai, Abways Technology, China, 1:500) and cleaved-Caspase 3 (AF7022, Affinity Biologicals, Melbourne, Australia, 1:500). Beta Tubulin (R380628, Zen BioScience, Chengdu, China, 1:5000) was used as an internal reference. Next, the membranes were incubated with the corresponding secondary antibodies for 1 h at room temperature and quantified using the Odyssey CLx Infrared Imaging System (LI-COR Biosciences, Lincoln, NE, USA).

2.24. RNA extraction and RT-qPCR analysis

Total RNA of hESCs and hESC-EVs was extracted using Trizol Reagent (15596-026, Invitrogen, Carlsbad, USA), and the concentration was determined by NanoDrop-2000 spectrophotometer (Thermo Fisher Scientific, Waltham, MA, USA). Reverse-cDNA synthesis was performed using the High-Capacity cDNA Reverse Transcription Kit (4368814, Applied Biosystems, Waltham, MA, USA), and SYBR Green PCR Master Mix (04913914001, Sigma−Aldrich, St. Louis, MO, USA) was used for mRNA quantification according to the manufacturer's guidelines. Quantitative RT-PCR was performed using the 7500 FAST Real-Time PCR System (Applied Biosystems, Waltham, MA, USA). The mRNA expression levels were normalized to U6 or 18S. The primer sequences of this experiment are listed in Table 2.

2.25. Statistical analysis

All statistical analyses were carried out using GraphPad Prism version 9.0 (GraphPad Software, Inc., San Diego, CA, USA). Data are expressed as mean ± standard error of the mean (SEM). Normality for datasets with $n \geq 6$ was assessed using the Shapiro−Wilk test. Based on data distribution and homogeneity of variance, the following statistical tests were applied: for normally distributed data passing homogeneity of variance tests, two-tailed Student's *t* test was used to compare two groups, One-way analysis of variance (ANOVA) followed by Tukey's *post hoc* multicomparison test was used to compare differences among multiple groups; for normally distributed data failing homogeneity of variance tests, Unpaired *t* test with Welch's correction or Welch ANOVA followed by Dunnett's T3 *post hoc* test was applied; for non-normally distributed or small sample size ($n< 6$) data, the Mann−Whitney test (two-tailed) was used for two groups, and Kruskal−Wallis, followed by false discovery rate (FDR) method of Benjamini and Hochberg test was used for multiple groups. All experiments were independently replicated at least three times (independent biological replicates). A value of $P< 0.05$ was considered statistically significant.

3. Results

3.1. Green light-mediated photobiomodulation enhances the cardioprotective activity of hESC-EVs

Firstly, hESC-EVs were isolated from the conditioned medium of untreated H9-hESCs *via* ultracentrifugation. Transmission electron microscopy (TEM) observations showed that hESC-EVs exhibited a typical cup-shaped vesicle structure (Supporting Information Fig. S1A). Meanwhile, nanoparticle tracking analysis (NTA) demonstrated a single bell-shaped distribution centered at 100 nm, confirming the successful purification of hESC-EVs (Fig. S1B). To determine the optimal intervention dose of hESC-EVs on CMs, we evaluated CM viability after treatment with various concentrations of hESC-EVs using a CCK-8 assay. The results showed that hESC-EVs enhanced CM viability in a dose-dependent manner, with the most pronounced effect observed at a final concentration of 3×10^9 particles/mL, which was selected for our follow-up studies (Fig. S1C). Subsequently, to assess whether PBM affects the bioactivity of hESC-EVs, we exposed hESCs to multiple wavelengths of light, including green (520 nm), red (630 nm), yellow (590 nm), and blue (470 nm). The same number of EVs collected from each irradiated group were then used to treat CMs for 48 h. As shown in Fig. S1D, EVs derived from hESCs exposed to green light at a power density of 2.5 mW/cm^2 significantly improved CM viability compared to non-light and other wavelengths of light-treated groups. To further determine the optimal irradiation duration, we evaluated the bioactivity of hESC-EVs under varying durations of green light exposure. CCK-8 assay revealed that EVs derived from hESCs exposed to green light for 30 min significantly improved CM viability compared to the same particles of EVs from other groups

Table 2 Primers used for qPCR.

Gene	Forward primer	Reverse primer
hsa-miR-423-3p	AAGCTTAAGCTCGGTCTGAGGC	ATCCAGTGCAGGGTCCGAGG
pri-miR-423-3p	GAGGAAATAAAGGAAGTTAGGCTGA	CGGGTTAGGAAGCAAGACTG
mmu-miR-423-3p	CCAGCTCGGTCTGAGGCCCTAT	ATCCAGTGCAGGGTCCGAGG
hsa-let-7b-5p	TGAGGTAGTAGGTTGTGTGGTT	CGCAGGGTCCGAGGTATTC
hsa-miR-30d-5p	CCAGGTTCTGTAAACATCCCCGA	ATCCAGTGCAGGGTCCGAGG
U6	GCTTCGGCAGCACATATACTAAAAT	CGCTTCACGAATTTGCGTGTCAT
PKM2	TGCGGTGGCTCTGGATACAAAG	ACAGGATGTTCTCGTCACACTTCTC
ZBTB7A	TGCGAGAAGGTGATTCAGGGTG	TTCCGCATGTGCACCTTCAGCT
18S	CCTGGATACCGCAGCTAGGA	GCGGCGCAATACGAATGCCCC

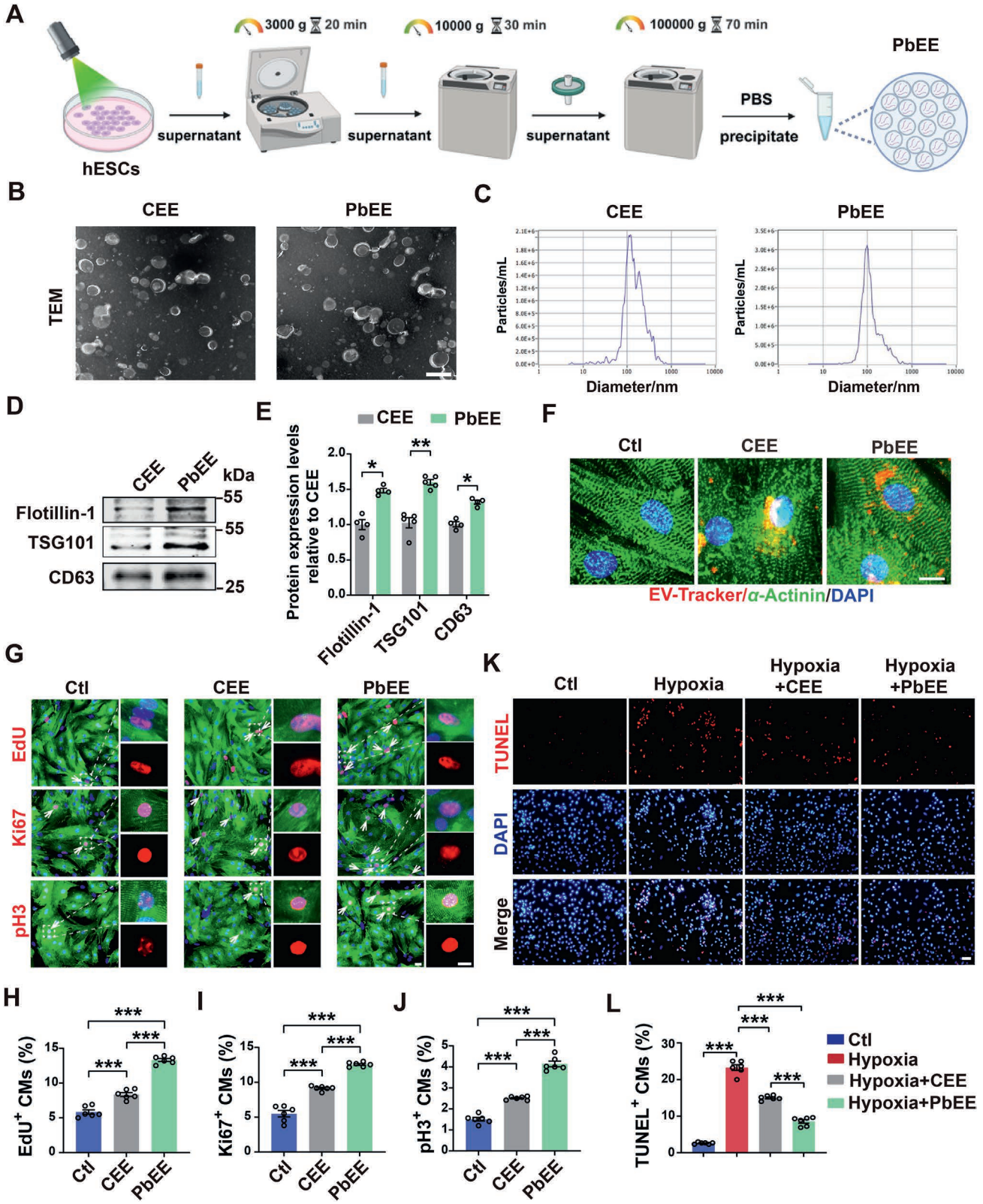

Figure 1 Green light induces human embryonic stem cells (hESCs) to secrete extracellular vesicles (EVs) with enhanced cardioprotective activity. (A) Preparation and extraction of photobiomodulation-reprogrammed hESC-EVs (PbEE). Created with BioRender.com. (B) Representative transmission electron microscopy (TEM) images of PbEE and control hESC-EVs (CEE). Scale bar, 200 nm. (C) Nanoparticle tracking analysis (NTA) of PbEE and CEE. (D, E) Western blot analysis of Flotillin-1, TSG101, and CD63 in EVs derived from equal numbers of H9-hESCs ($n = 4-5$). (F) Internalization of EV-tracker labeled EVs (red) by neonatal mouse cardiomyocytes after 12 h co-culture. Green: Alpha Actinin; blue: DAPI. Scale bar, 10 μm. (G–J) Representative images and quantification of cardiomyocyte proliferation assessed by EdU, Ki67,

(Fig. S1E). Subsequent NTA showed that EV production also peaked at 30 min (Fig. S1F). Therefore, 30 min of green light irradiation (520 nm, 2.5 mW/cm^2) was chosen to stimulate hESCs in our subsequent experiments, and these PBM-reprogrammed hESC-EVs were named as PbEE (Fig. 1A).

We further characterized the morphology of PbEE. Both TEM and NTA revealed that PbEE displayed comparable morphological features and particle size distribution to control hESC-EVs (CEE) (Fig. 1B and C). Western blot analysis showed that the levels of EV markers (Flotillin-1, TSG101, CD63) in PbEE were higher than those in CEE from the same number of H9-hESCs (Fig. 1D and E). Consistent results were obtained in H1-hESCs (Supporting Information Fig. S2A and S2B), further confirming that green light irradiation enhances the EV production of hESCs. To determine the biological activity of PbEE and CEE on CMs, we labeled these EVs using a membrane-specific fluorescent probe (EV-Tracker). After 12 h of incubation, red fluorescence signals of EVs were detected in the myocardial cytoskeleton (Fig. 1F). Similarly, green fluorescence from GFP-CD63-tagged EVs were also observed in CMs, indicating successful internalization of EVs (Supporting Information Fig. S3A and S3B). Subsequently, CMs were treated with equal particle numbers of CEE or PbEE for 48 h, respectively. Compared with CEE, PbEE significantly increased the positivity rates of the proliferation markers EdU, Ki67, and pH3 in CMs (Fig. 1G−J). Additionally, under hypoxic conditions, PbEE further reduced the number of TUNEL-positive CMs compared with CEE (Fig. 1K and L). The consistent results were further validated in PbEE derived from H1-hESCs (Supporting Information Fig. S4A−S4E). These findings indicate that PbEE has superior biological activity compared to the same number of CEE in promoting cell cycle activation and inhibiting CM apoptosis.

3.2. PbEE shows more potent pro-angiogenic activity than CEE in vitro

Given the critical role of angiogenesis in cardiac repair post-MI[35,36], we further compared the pro-angiogenic effects of PbEE and CEE on human umbilical vein endothelial cells (HUVECs). After incubation with Tracker probe-labeled EVs for 6 h, a pronounced red fluorescence signal was observed within HUVECs, indicating the endocytosis of EVs (Supporting Information Fig. S5A). Then, HUVECs were seeded on Matrigel-coated plates and treated with equal numbers of CEE and PbEE particles. Notably, PbEE-treated HUVECs were able to form more tubular networks than those treated with CEE (Fig. S5B−S5D, Supporting Information Fig. S6A−S6C). Consistently, wound healing assays showed that both CEE and PbEE enhanced the migration of HUVECs, with PbEE showing superior efficacy (Fig. S5E and S5F, Fig. S6D and S6E). These findings indicate that PbEE has a stronger pro-angiogenic potential than CEE *in vitro*.

3.3. PbEE exerts stronger therapeutic effects on mice with MI

To evaluate the therapeutic potential of CEE and PbEE in adult mice with MI, we administered various doses of these EVs (1×10^9, 3×10^{10}, and 9×10^{11} particles in 30 μL saline per animal) *via* intramyocardial injection following MI induction (Fig. 2A). Assessment of cardiac function at Day 28 revealed that 3×10^{10} particles induced the most significant functional improvement in both CEE and PbEE groups, with PbEE exhibiting superior efficacy than CEE at all doses (Supporting Information Fig. S7A and S7B, Fig. 2B and C). Based on this, 3×10^{10} particles/animal was chosen as the optimal concentration for further experiments. Histological analysis further demonstrated that PbEE treatment resulted in a significant reduction in infarct size compared to CEE (Fig. 2D and E). Moreover, PbEE therapy attenuated the MI-induced increase in heart-to-body weight ratio and CM cross-sectional area (Supporting Information Fig. S8A−S8C), indicating that PbEE has a stronger protective effect against adverse remodeling post-MI.

In addition, immunofluorescence staining revealed that PbEE treatment significantly increased the number of Ki67-, pH3-, and Aurora B-positive CMs in the border zone of infarcted hearts compared to the same particle number of CEE (Fig. 2F and G). PbEE also markedly elevated both the total number of adult CMs and the proportion of mononucleated CMs (Fig. 2H, Fig. S8D and S8E). No significant effect on CM proliferation was observed in the remote zone following either CEE or PbEE treatment (Supporting Information Fig. S9A−S9C). Consistent with the results obtained from NMCMs *in vitro*, PbEE treatment significantly reduced apoptotic CMs in the border zone relative to CEE (Fig. 2I). Moreover, while both CEE and PbEE enhanced angiogenesis, PbEE exhibited a greater pro-angiogenic effect than the same number of CEE (Fig. 2J). Collectively, these results suggest that PbEE possesses stronger cardioprotective effects against ischemic injury by promoting CM proliferation, inhibiting CM apoptosis, and stimulating angiogenesis.

3.4. PbEE exerts cardioprotective effects through miR-423-3p

It is well recognized that abundant small non-coding RNAs (sncRNAs) in EVs play key roles in mediating intracellular activities and intercellular communication. To further explore the molecular mechanism underlying the therapeutic effect of PbEE, we analyzed the differences in the expression profiles of sncRNAs, including miRNA, piRNA, tsRNA, rsRNA, and snoRNA, between the same particle number of CEE and PbEE by PANDORA-seq (Fig. 3A). As illustrated in Fig. 3B and C, compared with CEE, there was a notable increase of 11 sncRNAs and a decrease of 7 sncRNAs in the PbEE group ($P < 0.05$). Among these upregulated sncRNAs, 4 highly differentially expressed sncRNAs (hsa-miR-423-3p, hsa-let-7b-5p, piR-hsa-440814, and hsa-miR-30d-5p) were screened based on the fold change value ≥ 2. To verify the results of PANDORA-seq, we further detected the expression of these 4 sncRNAs in the two groups of EVs using qRT-PCR. The results showed that the expression of miR-423-3p in PbEE was significantly higher than that in CEE (Fig. 3D). Additionally, we also examined the expression of miR-423-3p in hESCs, and the results showed that compared with the untreated hESCs, the level of miR-423-3p in hESCs exposed to green light was significantly elevated (Supporting Information Fig. S10A). Thus, green light irradiation was able to upregulate miR-423-3p expression in hESCs and hESC-derived EVs.

and pH3 staining (red) after treatment with equal doses of CEE and PbEE (3×10^9 particles/mL; $n = 6$). White arrows: positive cells. Scale bars: 20 μm (main image) and 10 μm (magnification). (K, L) Representative TUNEL staining (red) and quantification of apoptotic cardiomyocytes ($n = 6$). Scale bar, 50 μm. Data are presented as mean ± SEM. *$P < 0.05$, **$P < 0.01$, ***$P < 0.001$.

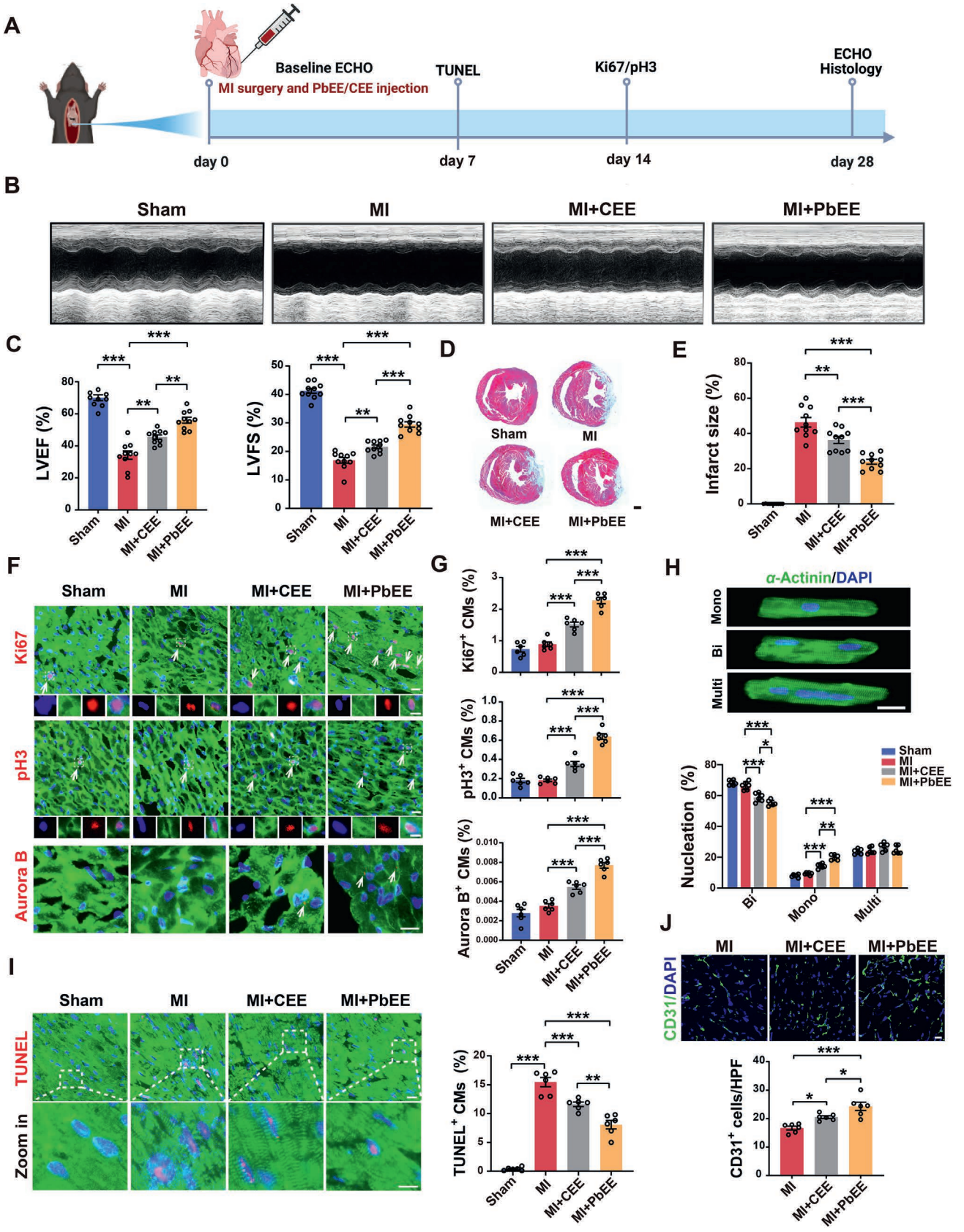

Figure 2 PbEE exhibits stronger cardioprotective effects than CEE in mice with myocardial infarction (MI). (A) Schematic of the *in vivo* experimental procedure (created with Biorender.com). ECHO: echocardiography. (B, C) Representative echocardiograms (B) and quantification of left ventricular ejection fraction (LVEF) and fractional shortening (LVFS) (C) on Day 28 post-MI. Mice received equal doses of CEE and PbEE

Subsequently, we detected the expression of miR-423-3p in CMs treated with an equal particle number of CEE and PbEE. The results showed that, compared with the CEE group, PbEE treatment significantly up-regulated miR-423-3p expression in CMs (Fig. S10B). Previous studies have shown that miR-423-3p, which is highly conserved in multiple species, mediates cell growth in hepatocellular carcinoma and gastric cancer[37,38]. However, whether miR-423-3p is involved in CM proliferation and heart regeneration after MI remains unclear. To further determine the potential roles of miR-423-3p in PbEE-mediated cardioprotection, we suppressed miR-423-3p expression in hESCs using antagomir following green light exposure. qRT-PCR assay verified the effective knockdown of miR-423-3p in both hESCs and their derived EVs. Subsequent immunofluorescence revealed a significant decrease in EdU-, pH3- and ki67-positive CMs in the PbEE-antagomir-miR-423-3p (PbEE-anta) group compared to the PbEE-NC group (Fig. 3E−H). This indicates that knockdown of miR-423-3p attenuated PbEE-induced CM proliferation. Furthermore, suppression of miR-423-3p significantly diminished the anti-apoptotic effect of PbEE, as evidenced by increased TUNEL-positive CMs, elevated expression of cleaved-Caspase 3 and Bax, and reduced Bcl2 levels in the PbEE-anta group compared to the PbEE-NC group (Fig. 3I−N). These results collectively demonstrate that miR-423-3p is the key molecule of PbEE in promoting CM proliferation and anti-apoptosis.

3.5. Green light upregulates miR-423-3p in hESCs and EVs via the TRP−Ca^{2+}−CAMKII−CREB signaling axis

Previous studies have shown that green light PBM can induce calcium influx *via* the transient receptor potential (TRP) channel, thereby activating calcium/calmodulin-dependent protein kinase II (CAMKII) and its downstream transcription factor cAMP response element-binding protein (CREB), which in turn regulates the transcription of target genes[39,40]. To investigate the upstream mechanism by which green light induces miR-423-3p upregulation in hESCs and their EVs, we first assessed its effect on intracellular calcium mobilization. Fluo-4 AM fluorescence assay revealed that green light irradiation significantly elevated intracellular calcium levels in hESCs, whereas this inductive effect was abrogated by TRP channel inhibitor SKF (Supporting Information Fig. S11A). Western blot analysis further revealed that green light enhanced phosphorylation of both CAMKII and CREB, which was also blocked by TRP channel inhibition (Fig. S11B). We next quantified miR-423-3p expression *via* qRT-PCR. Green light exposure markedly elevated levels of both pri-miR-423-3p and mature miR-423-3p in hESCs, and correspondingly increased mature miR-423-3p in EVs. These effects were reversed upon TRP channel inhibition (Fig. S11C−S11E), indicating that the TRP−Ca^{2+} pathway is essential for green light-induced miR-423-3p upregulation.

To determine whether CREB directly regulates miR-423-3p transcription, we conducted a luciferase reporter assay targeting the miR-423 promoter. CREB overexpression significantly enhanced luciferase activity (Fig. S11F), suggesting direct binding and transcriptional activation. Furthermore, CREB knockdown in hESCs resulted in a significant reduction of both pri-miR-423-3p and mature miR-423-3p (Fig. S11G and S11H), confirming its regulatory role. Collectively, these findings demonstrate that green light activates the TRP−Ca^{2+}−CAMKII−CREB axis to promote miR-423-3p transcription in hESCs, thereby increasing miR-423-3p abundance in EVs (Fig. S11I).

3.6. MiR-423-3p regulates CM cycle activation, CM apoptosis, and angiogenesis by targeting the ZBTB7A/PKM2 axis

To further investigate the molecular mechanism by which miR-423-3p promotes CM cell cycle activation, we performed bioinformatic analysis using TargetScan and TarBase algorithms to identify target genes with conserved binding sites for miR-423-3p. After matching the putative targets from both databases, we found that *Zbtb7a*, *Rap2c*, *Pabpc1*, and *Kctd2* were screened by both methods (Fig. 4A). It is recognized that promoting metabolic conversion to glycolysis can reverse CM cell cycle arrest[41,42]. In our study, we found a notable enhancement in CM glycolytic capacity following PbEE treatment, as assessed by the seahorse glycolysis stress test (Fig. 4B and C). Previous studies have shown that ZBTB7A, a member of the POZ/BTB and POK family of transcription factors, directly binds and represses the transcription of key glycolytic genes, including pyruvate kinase M2 (*Pkm2*), thereby regulating tumor progression[43-45]. However, whether ZBTB7A could mediate glycolytic metabolism in CMs and cardiac repair post-MI remains unclear. Therefore, we speculated that miR-423-3p in PbEE might promote CM glycolytic metabolism by downregulating ZBTB7A expression, thereby enabling CMs to re-enter the cell cycle.

In order to confirm this hypothesis, we first constructed luciferase reporter vectors carrying 3′UTR binding sites or mutated sites of *ZBTB7A* mRNA, respectively (Fig. 4D). The luciferase activity of wild-type *ZBTB7A* mRNA 3′UTR was suppressed upon co-transfection with miR-423-3p, while the reduction of luciferase activity was not present when 3′UTR binding sequence was mutated, suggesting that miR-423-3p could directly target 3′UTR of *ZBTB7A* (Fig. 4E). Then, to verify the relationship between miR-423-3p and ZBTB7A, we modulated miR-423-3p expression in CMs and found that overexpression of miR-423-3p reduced ZBTB7A protein levels, whereas inhibition of miR-423-3p increased the expression of ZBTB7A protein (Fig. 4F and G, Fig. S10C). These results proved that miR-423-3p directly targets and negatively regulates ZBTB7A expression in CMs. Additionally, we examined whether ZBTB7A could modulate

(3×10^{10} particles; $n = 10$). (D, E) Representative Masson's trichrome staining and quantification of infarct size on Day 28 post-MI ($n = 10$). The scale bar indicates 500 μm. (F, G) Representative images and quantification of cardiomyocyte proliferation assessed by Ki67, pH3, and Aurora B staining (red) in the infarct border zone at Day 14 post-MI ($n = 6$). Green: Alpha Actinin; blue: DAPI. White arrows: positive cardiomyocytes; boxed regions: magnified views. Scale bars: 20 μm (main image) and 10 μm (magnification). (H) Representative images and quantification of cardiomyocyte nucleation patterns (percentage of mononuclear, binuclear, and multinuclear cardiomyocytes) at Day 14 post-MI ($n = 6$). Scale bar, 20 μm. (I) Representative images and quantification of TUNEL-positive cardiomyocytes (red) in the infarct border zone on Day 7 post-MI ($n = 6$). Boxed regions: magnified views. 20 μm (main image) and 10 μm (magnification). (J) Immunofluorescence staining and quantification of CD31-positive capillaries (green) in the infarct border zone on Day 28 post-MI ($n = 6$). Blue: DAPI. Scale bar, 20 μm. Data are expressed as mean ± SEM. *$P < 0.05$, **$P < 0.01$, ***$P < 0.001$.

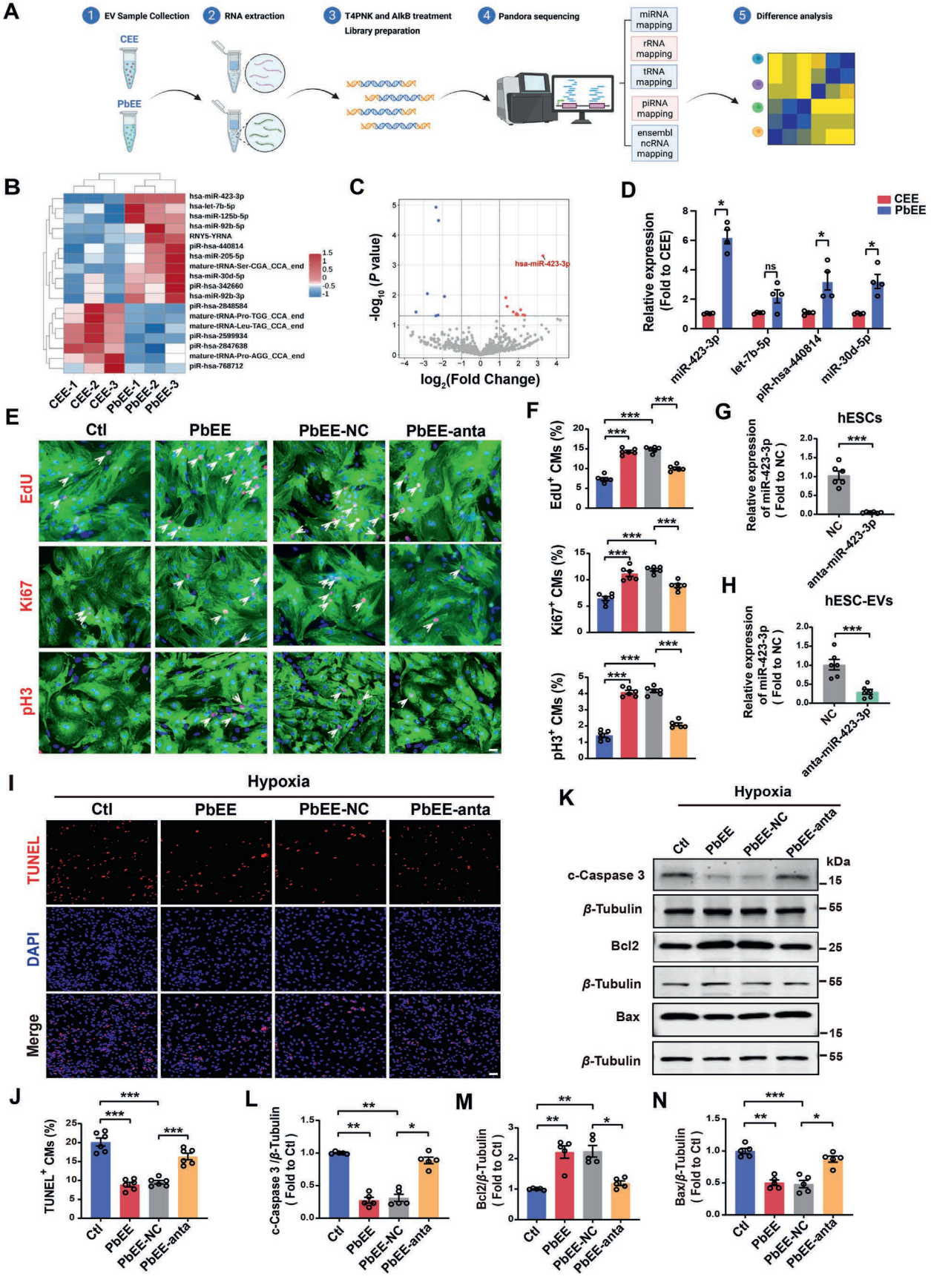
A
1 EV Sample Collection
2 RNA extraction
3 T4PNK and AlkB treatment
Library preparation
4 Pandora sequencing
5 Difference analysis
CEE
PbEE
miRNA mapping
rRNA mapping
tRNA mapping
piRNA mapping
ensembl ncRNA mapping
B
hsa-miR-423-3p
hsa-let-7b-5p
hsa-miR-125b-5p
hsa-miR-92b-5p
RNY5-YRNA
piR-hsa-440814
hsa-miR-205-5p
mature-tRNA-Ser-CGA_CCA_end
hsa-miR-30d-5p
piR-hsa-342660
hsa-miR-92b-3p
piR-hsa-2848584
mature-tRNA-Pro-TGG_CCA_end
mature-tRNA-Leu-TAG_CCA_end
piR-hsa-2599934
piR-hsa-2847638
mature-tRNA-Pro-AGG_CCA_end
piR-hsa-768712
CEE-1
CEE-2
CEE-3
PbEE-1
PbEE-2
PbEE-3
C
-log10 (P value)
log2(Fold Change)
hsa-miR-423-3p
D
CEE
PbEE
Relative expression (Fold to CEE)
miR-423-3p
let-7b-5p
piR-hsa-440814
miR-30d-5p
ns
E
Ctl
PbEE
PbEE-NC
PbEE-anta
EdU
Ki67
pH3
F
EdU+ CMs (%)
Ki67+ CMs (%)
pH3+ CMs (%)
G
hESCs
Relative expression of miR-423-3p (Fold to NC)
NC
anta-miR-423-3p
H
hESC-EVs
I
Hypoxia
TUNEL
DAPI
Merge
J
TUNEL+ CMs (%)
K
Hypoxia
c-Caspase 3
β-Tubulin
Bcl2
Bax
kDa
L
c-Caspase 3 /β-Tubulin (Fold to Ctl)
M
Bcl2/β-Tubulin (Fold to Ctl)
N
Bax/β-Tubulin (Fold to Ctl)

miR-423-3p′s regulatory role in CM proliferation. Immunofluorescence staining showed that overexpression of ZBTB7A suppressed the increase of EdU-, Ki67-, and pH3-positive CMs induced by miR-423-3p (Fig. 4H−K, Fig. S10D).

Subsequently, we further investigated whether miR-423-3p affects PKM2 expression *via* ZBTB7A, thus facilitating glycolysis in CMs. Fig. 4L and M showed that the mRNA and protein expression of PKM2 were markedly up-regulated due to the overexpression of miR-423-3p, but the forced expression of ZBTB7A reversed the promoting effect of miR-423-3p. Meanwhile, the seahorse glycolysis stress test was conducted to assess the roles of miR-423-3p and ZBTB7A on CM metabolism. The results displayed that forced expression of miR-423-3p enhanced the glycolytic capacity of CMs, while the simultaneous overexpression of ZBTB7A reversed the glycolysis-promoting effect of miR-423-3p (Fig. 4N and O). Collectively, these findings indicate that miR-423-3p inhibits ZBTB7A expression, which promotes *Pkm2* transcription, thereby elevating glycolytic metabolism in CMs and ultimately unlocking CM cell cycle arrest.

Furthermore, we found that overexpression of miR-423-3p in CMs markedly inhibited the CM apoptosis induced by hypoxia, indicated by the decreased TUNEL-positive CMs, decreased levels of cleaved-Caspase 3 and Bax, and up-regulated expression of Bcl2 (Fig. 5A−D). It is properly acknowledged that PKM2 not only acts as a promoter of aerobic glycolysis, but also as a regulator of mitochondrial homeostasis and cell survival[46,47]. In this study, JC-1 assay revealed that the reduction of CM mitochondrial membrane potential induced by hypoxia was notably preserved by the overexpression of miR-423-3p. However, the stabilizing effect of miR-423-3p on mitochondrial membrane potential was inhibited by overexpression of ZBTB7A or knockdown of PKM2 (Fig. 5E and F). Moreover, mitochondrial reactive oxygen species (ROS) production was markedly decreased in agomiR-423-3p group, which was also reversed by overexpression of ZBTB7A or knockdown of PKM2 in CMs (Fig. 5G and H). Additionally, we also found a notable rise in miR-423-3p and PKM2 expression, alongside a reduction in ZBTB7A levels in HUVECs treated with PbEE compared to the CEE group (Supporting Information Fig. S12A−S12C). Collectively, these results suggest that miR-423-3p maintains CM mitochondrial function, inhibits apoptosis, and promotes angiogenesis by targeting PKM2.

In order to further verify the role of miR-423-3p in cardiac repair post-MI, we administered agomir-miR-423-3p *via* tail vein injection in a mouse MI model. MI mice receiving agomir-miR-423-3p showed significantly improved cardiac function and reduced infarct size (Supporting Information Fig. S13A−S13D). Furthermore, the number of Ki67-and pH3-positive CMs was obviously increased in the agomir-miR-423-3p group (Fig. S13E−S13H). The number of TUNEL-positive CMs was also reduced in the agomir-miR-423-3p group (Fig. S13I and S13J). qRT-PCR analysis confirmed that systemic administration of agomir resulted in significant overexpression of miR-423-3p in heart tissue (Fig. S13K). Additionally, overexpression of miR-423-3p down-regulated the expression of ZBTB7A (Fig. S13L and S13N), while up-regulating the expression of PKM2 in heart tissues and adult CMs (Fig. S13M and S13O). The above findings suggest that overexpression of miR-423-3p can markedly ameliorate cardiac function post-MI by promoting CM survival.

3.7. Overexpression of ZBTB7A abrogates the cardioprotective effects of PbEE in vivo

To further investigate the role of ZBTB7A in the cardioprotective effects of PbEE, we induced cardiac-specific overexpression of ZBTB7A in MI mice treated with PbEE using a recombinant AAV9 system. As expected, overexpression of ZBTB7A (MI + PbEE + AAV9-ZBTB7A) largely abolished the therapeutic benefits of PbEE on cardiac contractility, as evidenced by the reduced EF% and FS% compared to the MI + PbEE + AAV9-NC group (Supporting Information Fig. S14A and S14B). Consistently, the reduction in infarct size induced by PbEE was also reversed by ZBTB7A overexpression (Fig. S14C and S14D). In addition, immunofluorescence staining of cardiac tissue showed that compared with the MI + PbEE + AAV9-NC group, overexpression of ZBTB7A significantly reduced the number of Ki67-positive CMs, increased the proportion of TUNEL-positive CMs, and reduced the signal intensity of CD31 (Fig. S14E−S14J). Western blot analysis revealed that PbEE treatment downregulated ZBTB7A and upregulated PKM2, whereas forced expression of ZBTB7A effectively blocked PbEE-induced PKM2 upregulation (Fig. S14K and S14L). These results demonstrate that ZBTB7A overexpression abolishes the cardioprotective effect of PbEE.

3.8. Characterization of the PbEE-loaded GelMA MN patch

While EVs hold therapeutic promise, their clinical translation is hampered by rapid clearance and poor retention at target sites. To enable sustained local delivery of PbEE to the infarcted myocardium, we fabricated a gelatin methacryloyl (GelMA) microneedle (MN) patch *via* a two-step template method (Fig. 6A). Optical microscopy revealed that the MN tips were conical and arranged in a precise array. The patch comprised 68 individual needles, which were uniformly distributed on a circular baseplate with a diameter of 0.6 cm (Fig. 6B). SEM showed that each MN tip was flat and intact, with a length of about 650 μm and a basal diameter of 320 μm (Fig. 6C). We next evaluated the mechanical properties of the MNs, which determine the ability of MNs to penetrate the myocardium. Fig. 6D shows that the mechanical strength of MNs was 0.4 N per needle, which was reported to be sufficient to penetrate the myocardium without fracture[48]. To visualize EV distribution within the hydrogel matrix, we incorporated fluorescently labeled PbEE into the MN patches. Both optical and

Figure 3 miR-423-3p mediates the cardioprotective effect of PbEE. (A) Schematic diagram of the Pandora sequencing process (created with Biorender.com). (B, C) Heatmap and Volcano plot of differentially expressed small non-coding RNAs (sncRNAs) between PbEE and CEE. Red: upregulated; blue: downregulated ($n = 3$). (D) qRT-PCR analysis of sncRNAs in PbEE and CEE ($n = 4$). (E, F) Representative images and quantification of cardiomyocyte proliferation assessed by EdU, Ki67, and pH3 staining ($n = 6$). Green: Alpha Actinin; blue: DAPI. White arrows: positive cardiomyocytes. Scale bar, 20 μm. (G, H) miR-423-3p levels in human embryonic stem cells (hESCs) and their extracellular vesicles (hESC-EVs) 48 h after antagomir-miR-423-3p transfection ($n = 6$). (I, J) Representative images and apoptosis index of cardiomyocytes treated with PbEE, PbEE-NC, or PbEE-antago-miR-423-3p (PbEE-anta) under hypoxia for 24 h ($n = 6$). Scale bar, 50 μm. (K−N) Western blot analysis of cleaved-Caspase 3, Bcl2, and Bax in hypoxic cardiomyocytes ($n = 5$). Data are presented as mean ± SEM. $^{*}P < 0.05$, $^{**}P < 0.01$, $^{***}P < 0.001$; ns, not significant.

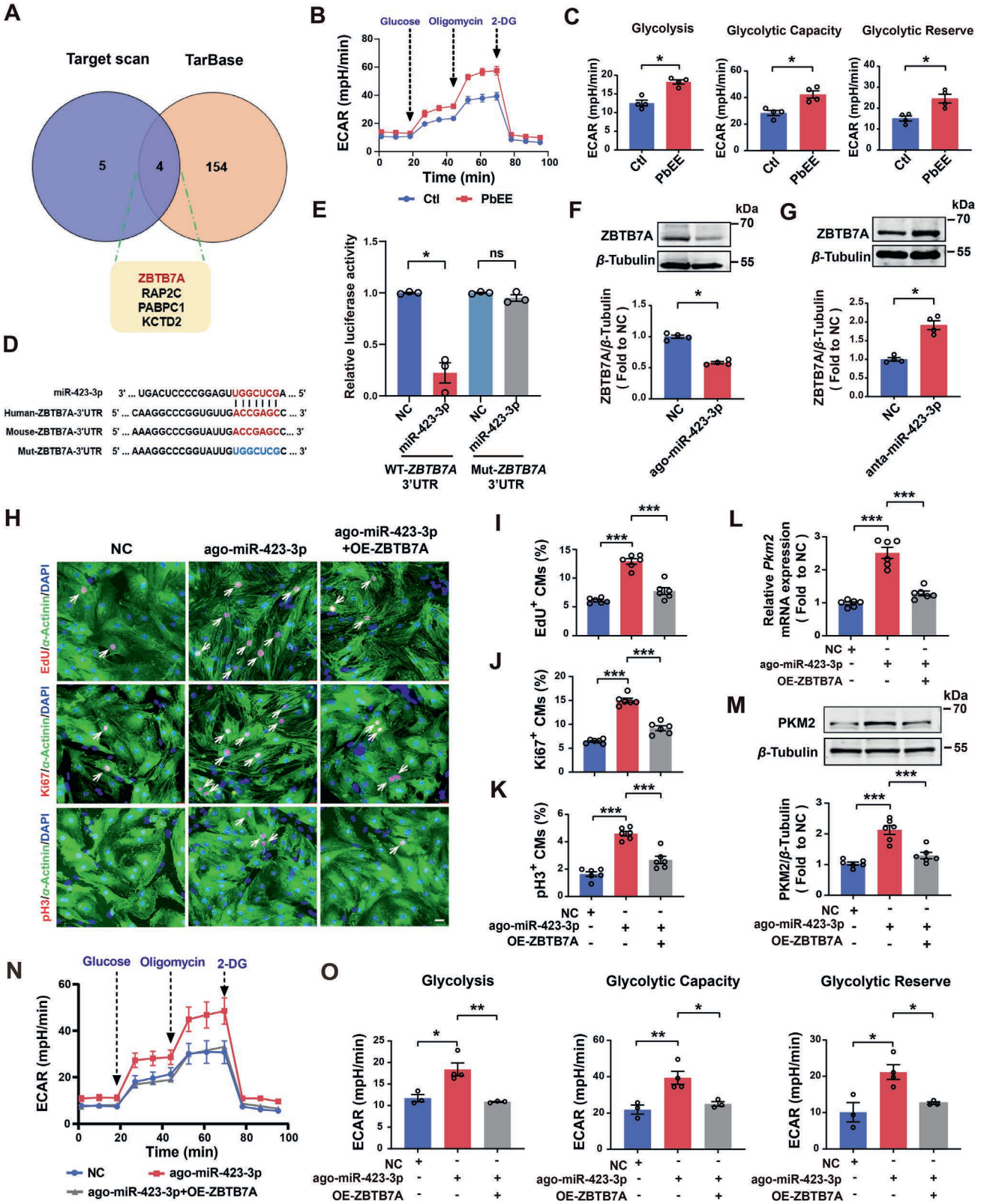

Figure 4 miR-423-3p promotes cardiomyocyte proliferation by targeting the ZBTB7A/PKM2 axis. (A) Bioinformatic prediction of miR-423-3p targets using TargetScan and TarBase. (B, C) Glycolysis stress test profiles and quantification of extracellular acidification rate (ECAR) in cardiomyocytes treated with or without PbEE for 48 h ($n = 4$). (D) Sequence alignment of conserved miR-423-3p binding sites in the 3′UTR of human and mouse *ZBTB7A* mRNA, and schematic of wild-type (WT) and mutant (Mut) luciferase reporter constructs. (E) Luciferase reporter assay in HEK293T cells co-transfected with miR-423-3p mimics and ZBTB7A-WT or -Mut vectors ($n = 3$). (F, G) Western blot analysis and quantification of ZBTB7A protein levels in cardiomyocytes ($n = 4$). (H−K) Representative immunofluorescence images and quantification of

fluorescence microscopy images confirmed the uniform distribution of EVs throughout the MN structure (Fig. 6E and F). Subsequently, an *in vitro* release study was conducted to characterize the release kinetics of EVs. The cumulative number of released EV particles was quantified at multiple time points using NTA. As shown in Fig. 6G, the release profile displayed an initial burst release within the first three days, followed by a prolonged sustained-release phase. These results indicate that the MN patch enables continuous delivery of PbEE over an extended period.

A critical consideration for therapeutic MN applications is whether the fabrication process compromises EV integrity and bioactivity. To address this, we compared PbEE retrieved from dissolved MNs (MN-PbEE) with native, unprocessed PbEE (NA-PbEE). Zeta potential analysis showed no significant difference in surface charge between MN-PbEE and NA-PbEE (Supporting Information Fig. S15A), suggesting preservation of membrane stability. TEM further confirmed that MN-PbEE maintained its characteristic cup-shaped morphology (Fig. S15B). To assess the integrity of intravesicular cargo, we quantified the expression level of miR-423-3p, the key functional miRNA in PbEE. No significant difference was observed between MN-PbEE and NA-PbEE (Fig. S15C). We then evaluated the cellular uptake and functional performance of MN-PbEE *in vitro.* Uptake assays revealed that MN-PbEE were internalized by CMs with an efficiency comparable to that of NA-PbEE (Fig. S15D). Functionally, MN-PbEE significantly enhanced CM proliferation and inhibited apoptosis to a similar extent as NA-PbEE (Fig. S15E and S15F). Furthermore, there was no significant difference in the pro-angiogenic ability between the two groups of EVs (Fig. S15G and S15H). These results demonstrate that the bioactivity of PbEE is maintained following MN fabrication.

We next evaluated whether MN-mediated delivery could further enhance the therapeutic efficacy of PbEE compared with conventional direct incubation. Primary CMs were treated with PbEE *via* either direct incubation or MN-mediated delivery for 3−7 days (Fig. 6H). Subsequent analysis showed that PbEE loaded in MNs (PbEE@MN) exerted a more significant inhibitory effect on CM apoptosis compared to direct PbEE incubation (Fig. 6I and J). Consistently, PbEE@MN further increased the proportions of Ki67- and pH3-positive CMs relative to direct PbEE treatment, indicating enhanced promotion of CM proliferation (Fig. 6K−M). To further evaluate the clinical translational potential of PbEE, we extended our studies to cardiomyocytes derived from hESCs (hESC-CMs) (Fig. 7A and B). Consistent with primary NMCMs, PbEE showed stronger anti-apoptotic and cell-cycle-activating activities in hESC-CMs than CEE. Importantly, the therapeutic efficacy of PbEE@MN was superior to that of free PbEE (Fig. 7C−F). The above findings suggest that PbEE encapsulated within the MNs exhibits good stability and exerts sustained beneficial effects on CM apoptosis and cell cycle activation.

3.9. Therapeutic effects of PbEE@MN on mice with MI

Based on *in vitro* studies confirming that MNs can effectively load and release PbEE, we further evaluate the therapeutic potential of PbEE@MN (loaded with 3×10^{10} PbEE particles) for MI in adult mice through the experimental procedure shown in Fig. 8A. The MN patch was placed on a pump head apparatus connected to a vacuum. By holding the apparatus on the infarcted hearts for 5 s, the MN tips were fully inserted into the myocardium without shedding (Fig. 8B and C). H&E staining showed the pinholes where the MN tips penetrated the myocardial tissue (Fig. 8D). To assess the *in vivo* degradation of the MN patch, images of the patch on the heart surface were acquired at 3, 7, and 14 days post-implantation. The images showed a time-dependent decrease in structural integrity, with the patch becoming nearly undetectable by Day 14 (Supporting Information Fig. S16). This observation was further validated by Masson's trichrome staining (Fig. 8E and F), confirming the biodegradable nature of the MN patch. To assess the cardiac safety of MNs, cardiac tissue penetrated by empty MNs was compared with normal cardiac tissue (Ctl). H&E staining revealed no abnormal inflammatory infiltration or structural alterations in the MN-treated hearts (Fig. 8G). qRT-PCR further confirmed that there were no significant differences in the expression of inflammatory factors *Tnfa*, *Il1b*, and *Il6* between the MN-treated group and the Ctl group (Fig. 8H), indicating good biocompatibility of MNs. To determine the retention rate of PbEE in mouse myocardium, we used Tracker probe-labeled EVs to observe the fluorescence signals in the heart at different time periods after intramyocardial injection of PbEE and PbEE@MN treatment. On Day 3, the EV fluorescence intensity in the PbEE@MN group was significantly higher than that in the PbEE group. On Day 14, the signal was no longer present in the hearts injected with PbEE, but remained evident in the hearts treated with PbEE@MN (Fig. 8I). These results indicate that the prepared MN patches are capable of continuously and effectively delivering PbEE to the myocardial ischemic area.

Subsequently, we evaluated the therapeutic effects of PbEE@MN on infarcted hearts. The results showed that animals treated with PbEE@MN (loaded with 3×10^{10} PbEE particles) exhibited more significant improvements in cardiac function, heart weight to body weight ratio, infarct size, and CM cross-sectional area than those receiving myocardial injection of PbEE (Fig. 8J−N, Fig. 9A and B). Immunofluorescence staining and stereological analysis revealed that the number of Ki67-, pH3-, and Aurora B-positive CMs, the proportion of mononuclear CMs, and the total number of CMs were markedly increased in the PbEE@MN group compared to the PbEE-injected group (Fig. 9C−E, Supporting Information Fig. S17A−S17C). Furthermore, TUNEL analysis revealed that PbEE@MN exerted a stronger anti-apoptotic effect than direct PbEE injection, as indicated by a significant reduction in apoptotic CMs (Fig. 9F). Meanwhile, PbEE@MN further promoted angiogenesis in the infarcted heart compared with the PbEE-injected group (Fig. 9G). Taken together, these data suggest that MN patches indeed improve the therapeutic effects of PbEE by sustained release of EVs for a longer period.

To further confirm the critical role of miR-423-3p/ZBTB7A/PKM2 axis in PbEE@MN-mediated cardioprotection, we examined the expression of ZBTB7A and PKM2 in MI hearts following PbEE and PbEE@MN treatment. The results showed that PbEE@MN significantly inhibited ZBTB7A expression and up-regulated PKM2

cardiomyocytes positive for EdU, Ki67, and pH3 ($n = 6$). Green: Alpha Actinin; blue: DAPI. White arrows: proliferating cardiomyocytes. Scale bar, 20 μm. (L, M) PKM2 expression at the mRNA and protein levels was assessed by qRT-PCR and Western blot ($n = 6$). (N, O) Seahorse analysis of glycolysis in cardiomyocytes following modulation of miR-423-3p and ZBTB7A levels ($n = 3$−4). Data are presented as mean ± SEM. *$P < 0.05$, **$P < 0.01$, ***$P < 0.001$; ns, not significant.

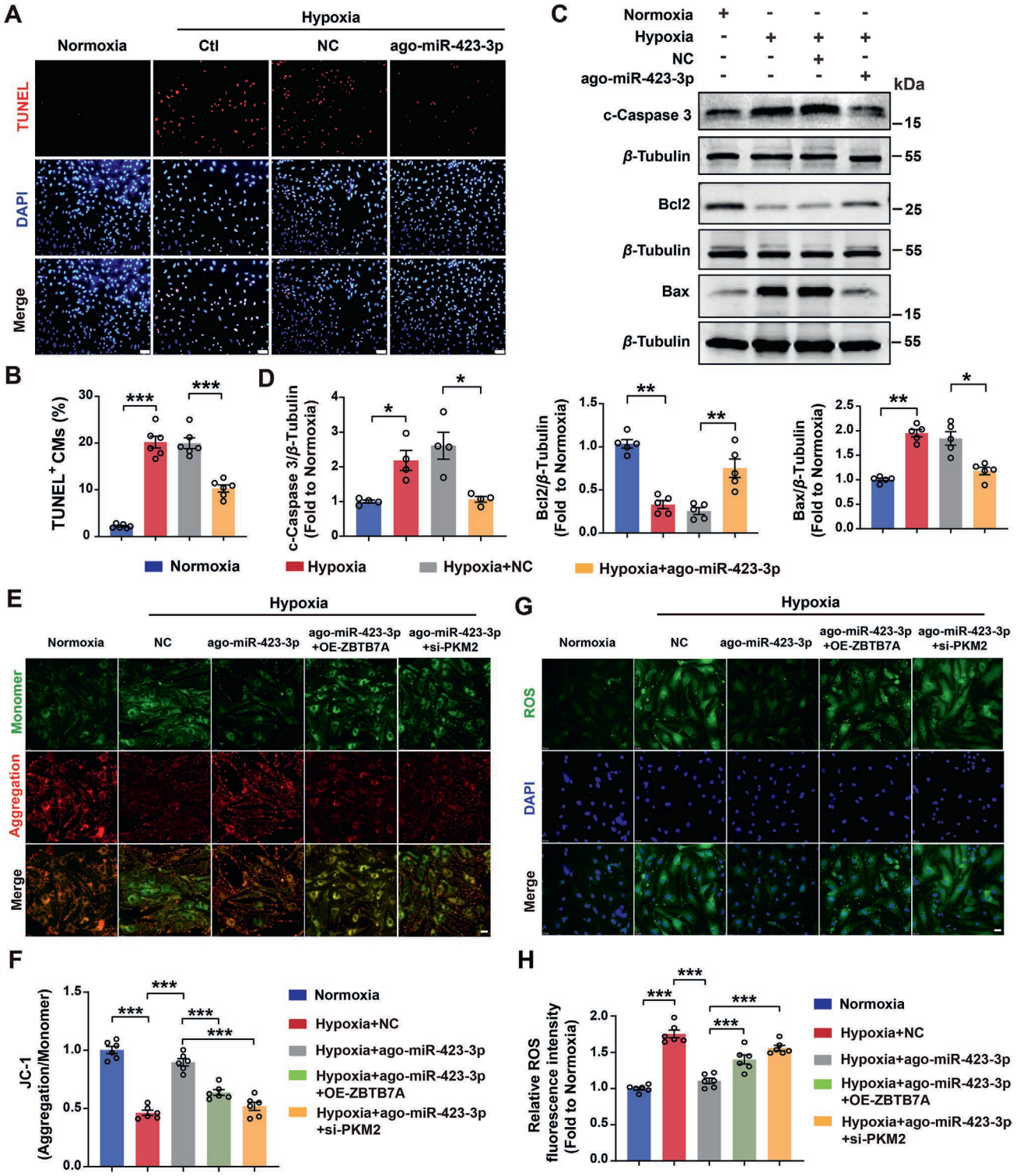

Figure 5 miR-423-3p inhibits cardiomyocyte apoptosis by up-regulating PKM2. (A, B) Representative TUNEL staining and quantification of apoptotic cardiomyocytes after 24 h of hypoxia, with or without miR-423-3p overexpression ($n = 6$). Scale bar, 50 μm. (C, D) Western blot analysis of cleaved-Caspase 3, Bcl2, and Bax protein levels in hypoxic cardiomyocytes following miR-423-3p overexpression ($n = 4–5$). (E) Representative JC-1 fluorescence images of cardiomyocytes co-transfected with agomir-miR-423-3p and ZBTB7A overexpression vector or PKM2 siRNA. Red: aggregation; green: monomer. Scale bar, 25 μm. (F) Quantification of the JC-1 aggregation/monomer fluorescence intensity ratio ($n = 6$). (G, H) Representative images and quantification of intracellular reactive oxygen species (ROS, green) in cardiomyocytes ($n = 6$). Scale bar, 25 μm. Data are expressed as mean ± SEM. *$P < 0.05$, **$P < 0.01$, ***$P < 0.001$.

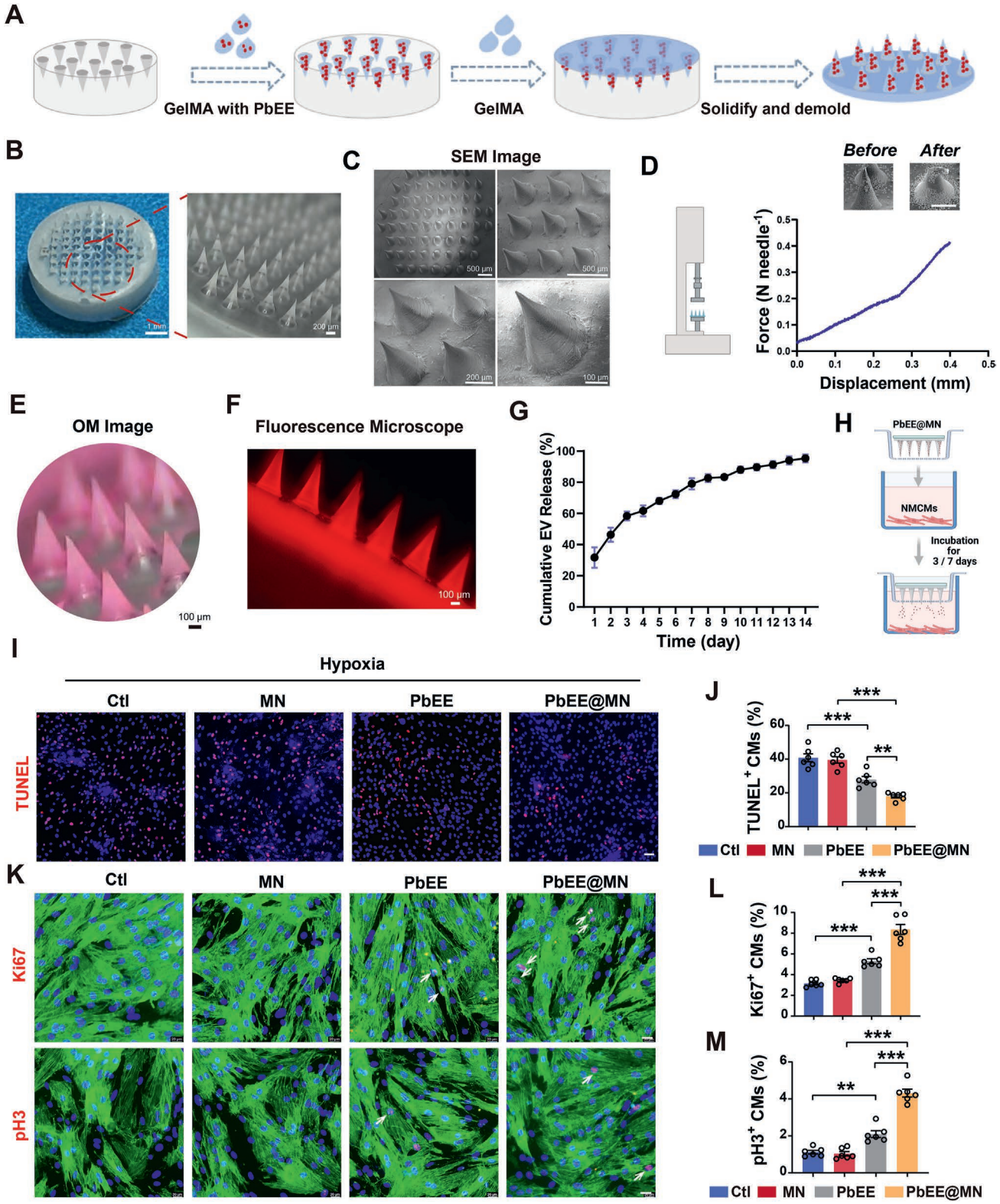

Figure 6 Preparation and characterization of gelatin methacryloyl (GelMA) microneedle (MN) patch. (A) Schematic illustration of the GelMA MN fabrication process. (B) Macroscopic digital images of the whole MN patch (left) and a magnified view of individual needles (right). Scale bars: 1 mm (left), 200 μm (right). (C) Representative scanning electron microscopy (SEM) images showing MN morphology at different magnifications. (D) Mechanical characterization (stress-strain curves) of MN patches under compression testing. Scale bar: 200 μm. (E, F) Optical and fluorescence microscopic images of MN patches loaded with Tracker probe-labeled PbEE (red). (G) The cumulative release profile of PbEE from MN patches over time, quantified by nanoparticle tracking analysis (NTA) ($n = 3$). (H) Schematic of the co-culture system involving MN patches and hypoxic cardiomyocytes (created with BioRender.com). (I, J) Representative TUNEL staining and quantification of apoptotic

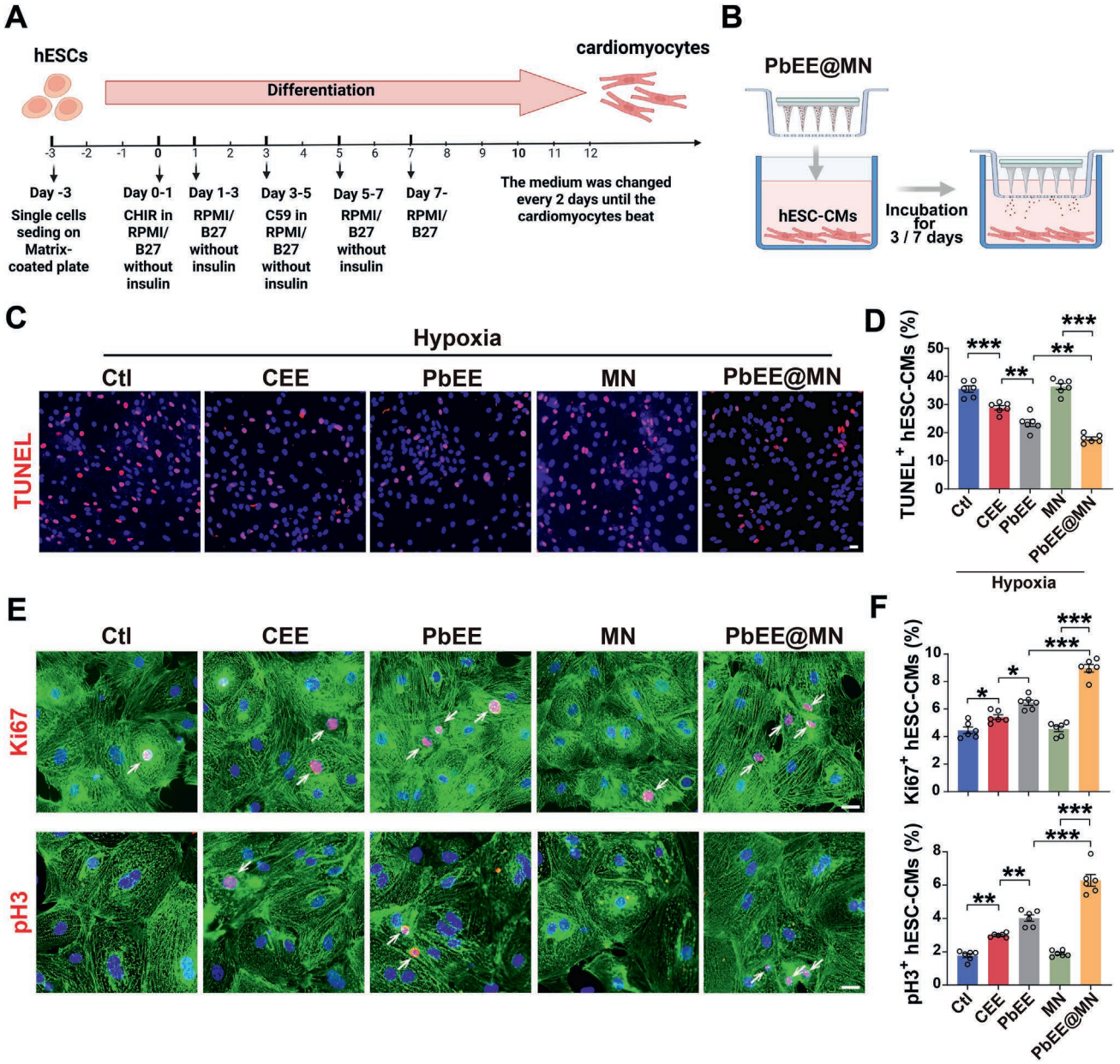

Figure 7 PbEE@MN promotes proliferation and inhibits apoptosis of human embryonic stem cell-derived cardiomyocytes (hESC-CMs). (A) Schematic illustration of the hESC-CM differentiation protocol (created with BioRender.com). (B) Schematic illustration of the co-culture experimental design involving PbEE@MN and hESC-CMs. (C, D) Representative TUNEL staining and quantification of apoptotic hESC-CMs after 3 days of hypoxia treated with MN alone, CEE, PbEE, or PbEE@MN ($n = 6$). Blue: DAPI. Scale bar, 20 μm. (E, F) Representative immunofluorescence images and quantification of $Ki67^+$ and $pH3^+$ hESC-CMs after 7 days of co-culture ($n = 6$). White arrows: positive proliferative signals. Scale bar, 20 μm. Data are presented as mean ± SEM. $^*P < 0.05$, $^{**}P < 0.01$, $^{***}P < 0.001$.

protein levels in heart tissue (Fig. 9H and I). Then, PbEE with knockdown of miR-423-3p was loaded into MNs (PbEE-anta@MN) and its effect on cardiac repair was evaluated. We found that silencing miR-423-3p partially eliminated the protective effect of PbEE@MN on myocardial injury (Supporting Information Fig. S18A−S18J). These findings indicate that miR-423-3p is a key molecule in PbEE@MN-mediated cardioprotection.

3.10. Safety assessment of PbEE@MN treatment

Given the potential tumorigenic risk associated with certain miRNAs in EVs, which may compromise therapeutic efficacy[49], we further evaluated the safety profile of PbEE-based therapy. Histological examination *via* H&E staining revealed no morphological abnormalities in heart tissues treated with PbEE@MN for

cardiomyocytes after 3 days of hypoxia and co-incubation with MN alone, free PbEE, or PbEE-loaded MN (PbEE@MN) ($n = 6$). Blue: DAPI. Scale bar, 50 μm. (K−M) Representative immunofluorescence images and quantification of Ki67-and pH3-positive cardiomyocytes after 7 days of treatment ($n = 6$). White arrows: positive proliferative signals. Scale bar, 20 μm. Data are presented as mean ± SEM. $^{**}P < 0.01$, $^{***}P < 0.001$.

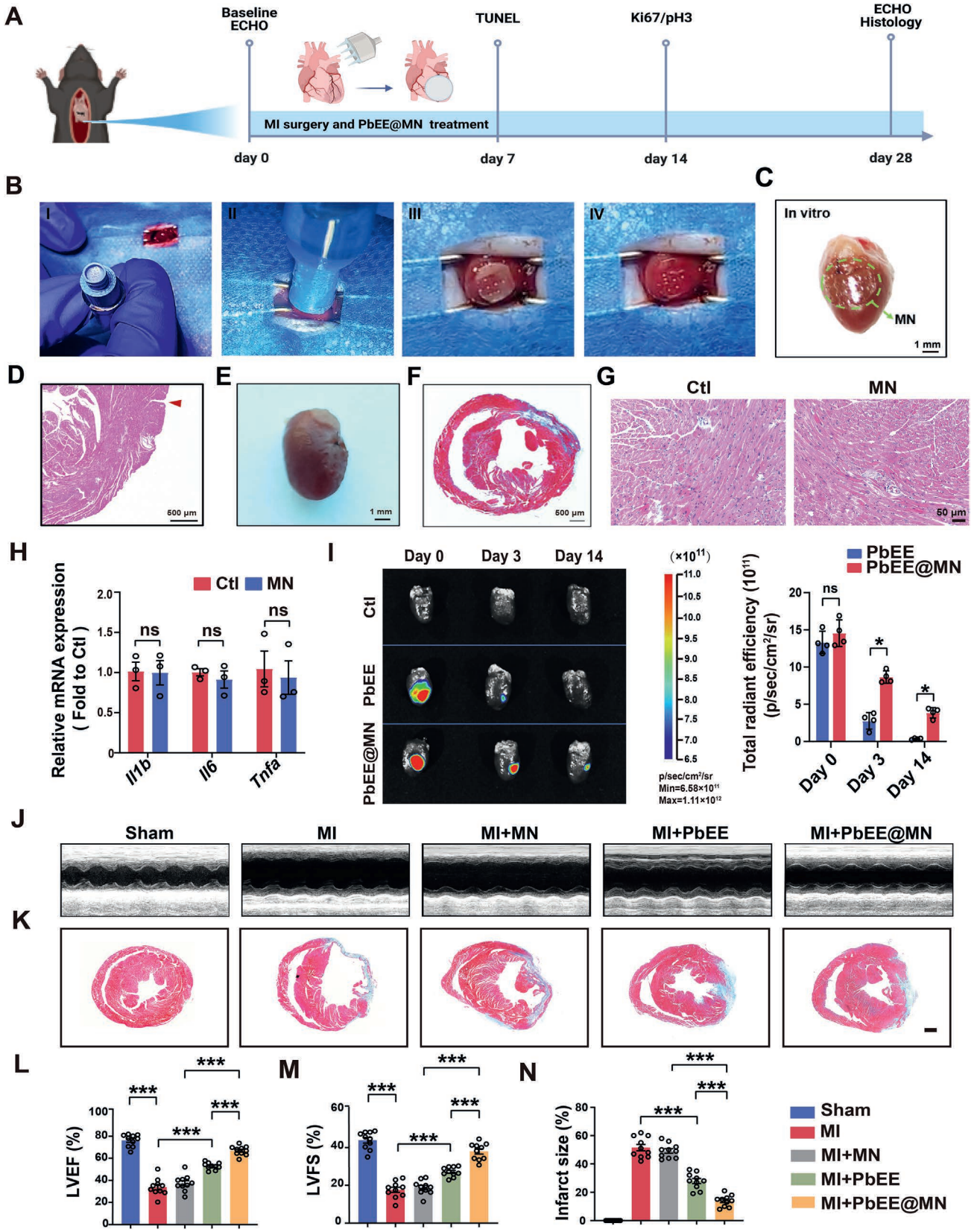

Figure 8 GelMA MN patches prolong PbEE residence time and enhance therapeutic efficacy in MI. (A) Schematic of the *in vivo* study design (created with BioRender.com). (B) Macroscopic images showing application of PbEE-loaded MN patches to the MI heart. Panels III and IV indicate attachment at 5 and 10 min post-application. (C) Stable attachment of the MN patch on Day 3 post-implantation. Scale bar, 1 mm. (D) Representative H&E staining showing MN penetration into myocardial tissue. Scale bar, 500 μm. (E) Macroscopic view of the heart on Day 28

6, 8, and 10 weeks (Fig. 9J). Consistent with these findings, qRT-PCR analysis of established cardiac tumor markers, including *Desmin*, *Vimentin*, and *Calb2,* showed no significant upregulation compared with the control group (Fig. 9K), indicating the absence of tumorigenic activity during the 10-week treatment period. Furthermore, *in vitro* release studies demonstrated that nearly all EVs were released from the MN system after 14 days (Fig. 9L), suggesting minimal risk of long-term retention. In addition, H&E staining of liver, spleen, kidney, brain, and lung tissues showed no significant cell death or inflammatory infiltration, supporting multi-organ safety (Fig. 9M). Together, these results demonstrate that PbEE-loaded GelMA MN patches represent a safe and effective strategy for enhancing cardiac regeneration and repair following MI.

4. Discussion

Recently, regenerative medicine based on stem cell-derived EVs has brought hope for the treatment of MI, because EVs not only retain the biological functions similar to stem cells, but also have the advantages of good permeability and low immunogenicity[50]. Nevertheless, the production of highly bioactive EVs and their effective delivery into the heart are major challenges for EV applications[51]. In this study, we revealed that green light irradiation could activate hESCs to reprogram EVs (PbEE), which exerted a stronger cardioprotective effect in MI mice. Mechanistically, we identified miR-423-3p in PbEE as a key regulator of cardiac repair, enhancing PKM2 levels by down-regulating the transcriptional inhibitor ZBTB7A, thereby promoting glycolysis and maintaining mitochondrial homeostasis, and ultimately activating cell cycle reentry of CMs, inhibiting apoptosis, and promoting angiogenesis. In addition, we synthesized GelMA MN patches to enable sustained release of PbEE in the infarcted area, thereby fully utilizing its cardioprotective effects. These findings provide new perspectives on therapeutic strategies for cardiac repair post-MI.

Routinely cultured stem cells secrete limited amounts of EVs, making it difficult to meet the requirements of industrial production and widespread clinical applications. In previous studies on the modulation of EV secretion, most methods either improved the biological activity of the obtained EVs or augmented their quantity[19]. However, the simultaneous enhancement of EV secretion and bioactivity has rarely been reported. Inspired by this, we aim to develop a safe and effective approach to stimulate stem cells to secrete more EVs with higher therapeutic activity. PBM is a non-invasive light-based therapy that triggers positive biological responses in cells and tissues. In recent years, PBM has been widely used clinically for its efficacy in wound healing, pain, muscle and nerve tissue remodeling, and anti-inflammation[21]. Notably, different wavelengths of light modulation may produce different effects. For instance, red light (peaked at 630 nm) is mainly used for tissue wound healing and the treatment of skin inflammation[52]. Blue light (peaked at 470 nm) is commonly used to inhibit tumor invasion and metastasis[53]. However, it remains unclear whether PBM affects the bioactive or yield of EVs secreted by stem cells. In this study, we demonstrate for the first time that green light (520 nm, 2.5 mW/cm^2) can activate hESCs to produce higher bioactive EVs, which significantly promote CM proliferation and inhibit CM apoptosis. In addition, compared with conventionally cultured hESCs, green light irradiation increased EV production by 1.4-fold without altering EV characteristics, including morphology and size distribution.

The presence of abundant sncRNAs in EVs, including miRNAs, piRNAs, tsRNAs, and rsRNAs, plays a pivotal role in promoting intercellular communication and signaling transduction. To explain why green light stimulation leads to greater cardioprotective activity of the obtained EVs, we analyzed the differential expression profiles of sncRNAs across EVs, revealing the most substantial upregulation in miR-423-3p. Despite the highest rsRNA abundance, the analysis showed no significant difference in rsRNA expression patterns between the two groups. Therefore, we hypothesized that the greater bioactivity of PbEE in cardiac repair was mainly due to the upregulation of miR-423-3p. Previous studies have shown that miR-423-3p, which is highly conserved in multiple species, mediates cell growth in hepatocellular carcinoma and gastric cancer[37,38]. Luo et al.[54] showed that miR-423-3p in fibroblasts can inhibit CM apoptosis and alleviate hypoxic reperfusion injury. Similarly, our findings indicate that miR-423-3p plays an indispensable role in PbEE-mediated cardiac repair post-MI. Mechanistically, we demonstrated that miR-423-3p down-regulates ZBTB7A, increases PKM2 and glycolytic metabolism in CMs, thereby promoting CM proliferation and inhibiting apoptosis.

Adult mammals face challenges in heart regeneration due to postnatal CM cycle arrest. However, reprogramming CM metabolism to glycolysis provides new insights into cardiac regeneration and repair post-injury[41,45]. Fukuda et al.[42] revealed that the expression of genes related to glycolysis was significantly upregulated in the proliferative boundary region of zebrafish with freeze injury. Following cardiac injury, the heart tends to rely on glycolysis as a source of energy, and PKM2 plays a key role in this process. As a rate-limiting enzyme in glycolysis, PKM2 can enhance glycolytic flux, which not only generates ATP to meet energy requirements but also diverts glycolytic intermediates into anabolic pathways such as the pentose phosphate pathway (PPP), thereby providing essential biosynthetic substrates for CM proliferation. In the nucleus, PKM2 functions as a transcriptional coactivator that interacts with beta-catenin, which in turn upregulates the expression of pro-proliferative genes, including *Ccnd1* and *Myc*, further promoting cell cycle progression[42,55,56]. Moreover, PKM2 exerts anti-apoptotic effects through metabolic reprogramming and mitochondrial protection. By promoting NADPH production, PKM2 enhances ROS scavenging capacity and

post-MN treatment. Scale bar, 1 mm. (F) Representative Masson's trichrome staining of MN-treated hearts on Day 28. Scale bar, 500 μm. (G) H&E staining was used to detect abnormal inflammatory infiltration or structural changes in the heart of the MN-treated group. Scale bar, 50 μm. (H) The mRNA expression of inflammatory factors *Tnfa*, *Il1b*, and *Il6* was analyzed by qRT-PCR ($n = 3$). (I) Bioluminescence imaging (BLI) tracking of EVs in hearts on Days 0, 3, and 14 post-MI ($n = 4$). (J) Representative M-mode echocardiograms on Day 28 following PbEE or PbEE@MN treatment. (K) Representative Masson's trichrome staining of infarct areas on Day 28. Scale bar, 500 μm. (L, M) Quantification of left ventricular ejection fraction (LVEF) and fractional shortening (LVFS) ($n = 10$). (N) Quantification of infarct size ($n = 10$). Data are shown as mean ± SEM. $^*P < 0.05$, $^{**}P < 0.01$, $^{***}P < 0.001$; ns, not significant.

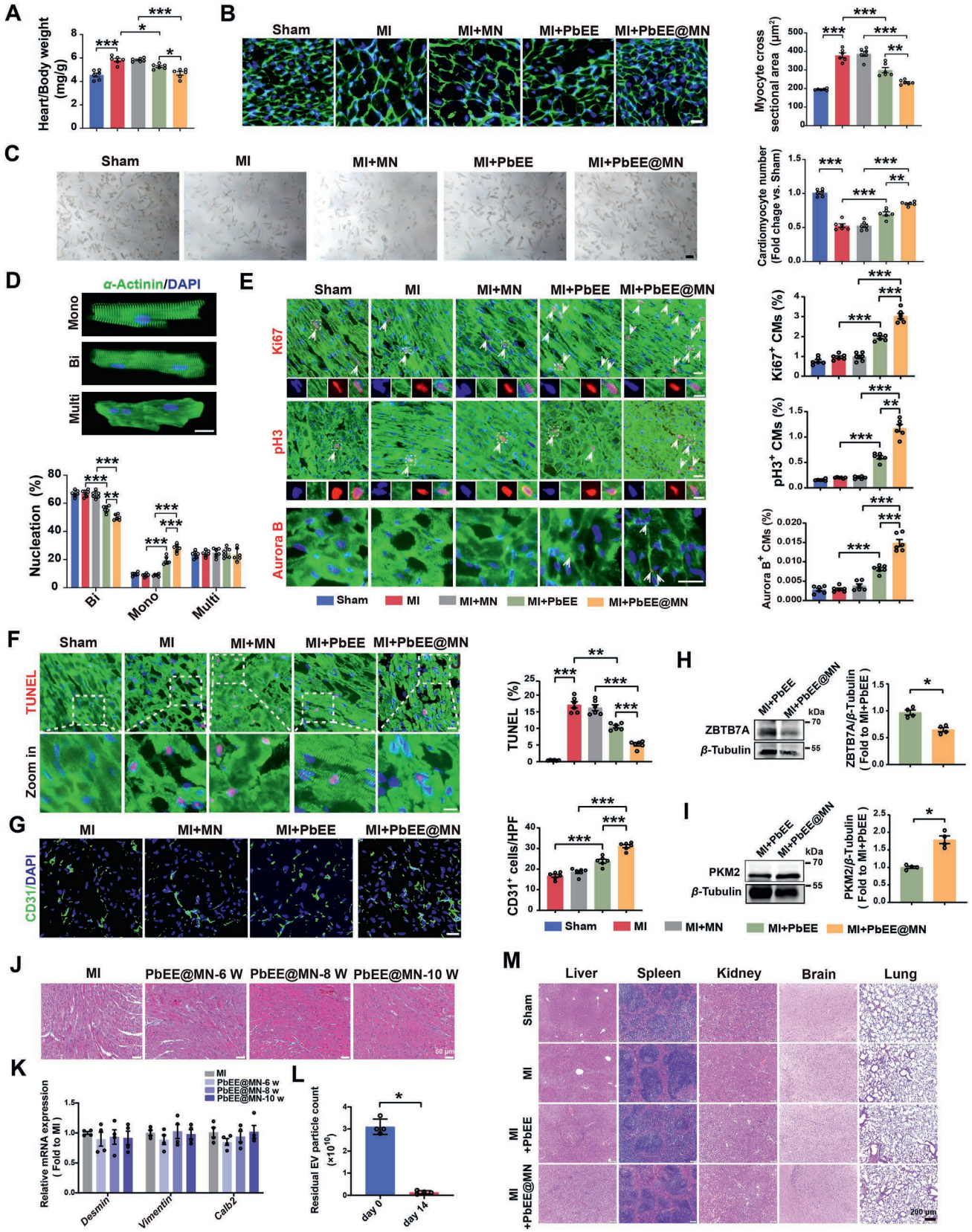

Figure 9 PbEE administration *via* MN patches promotes cardiac recovery and exhibits biocompatibility. (A) Heart weight to body weight ratio on Day 28 post-MI ($n = 6$). (B) Representative wheat germ agglutinin (WGA) staining (green) and quantification of cardiomyocyte cross-sectional area ($n = 6$). Scale bar, 20 μm. (C) Representative images and quantification of isolated cardiomyocytes ($n = 6$). Scale bar, 100 μm. (D) Representative images and quantification of cardiomyocyte nucleation patterns (percentage of mononuclear, binuclear, and multicore

preserves mitochondrial integrity[55,57]. Nuclear PKM2 further inhibits apoptosis by activating beta-catenin/TCF4 signaling cascades, which mediates the expression of *Myc* and *Sgk1*[58]. Additionally, Mitochondrial PKM2 can stabilize Bcl2, thereby suppressing oxidative stress-induced apoptosis. These dual roles underscore PKM2 as a pivotal regulator of CM renewal and viability[59]. Based on the presence of multiple conserved binding sites between ZBTB7A and the *Pkm2* DNA promoter region, we further probed the regulatory effects of miR-423-3p and ZBTB7A on mitochondrial glycolysis. We found that increasing miR-423-3p upregulated the mRNA and protein levels of PKM2, thereby promoting glycolysis and CM survival. However, these metabolic improvements were abolished by ZBTB7A overexpression. These data emphasize that miR-423-3p carried by PbEE exerts cardioprotective effects by mediating glycolytic metabolism *via* the ZBTB7A/PKM2 axis. To the best of our knowledge, this is the first study to highlight the metabolic regulatory effect of miR-423-3p in myocardial protection.

Mounting evidence indicates that stem cell-derived EVs have significant therapeutic potential for heart ischemic injury. Unfortunately, the treatment outcomes were highly variable due to unreliable EV delivery strategies. Local high-dose intramyocardial injection of EVs tends to trigger inflammatory responses and elevate the risk of thrombosis. This could also disrupt intercellular junctions at CMs, thereby affecting cardiac contractile function and electrical conduction[60]. Consequently, a secure and effective way to deliver EVs to the damaged myocardium and extend their residence time *in vivo* is key to improving the efficacy of EV transplantation. GelMA MN patch is an emerging efficient, safe, and convenient physical permeation technology, which is cross-linked to form a three-dimensional mesh structure that provides a platform for efficient loading and slow release of biomolecules[61,62]. Meanwhile, the GelMA MN patch also has certain compressive and tensile properties, providing mechanical support to injured myocardial tissue, thereby preventing heart rupture[63]. In this study, we encapsulated PbEE within GelMA MN patches to construct a stable EV delivery system. Furthermore, we designed a delivery device for MN patch fixation, addressing the challenge that conventional approaches cannot rapidly and directly implant MN patches onto the cardiac surface due to high heart rate. The results showed that MN patches prolonged the residency of PbEE in infarcted myocardium. As expected, compared with direct intramyocardial injection, PbEE@MN significantly promoted cardiac regeneration and restoration of cardiac function in infarcted mice. Furthermore, H&E staining of liver, spleen, kidney, brain, and lung sections revealed no obvious cell necrosis or inflammatory cell infiltration in these tissues following PbEE@MN treatment, suggesting that PbEE@MN administration poses no significant safety risks to major organs.

5. Conclusions

In summary, the present study systematically characterized the cardioprotective properties of PbEE, a novel EVs derived from hESCs under green light irradiation. Our findings revealed that PbEE exhibited superior protective efficacy against myocardial ischemic injury compared to natural EVs. Mechanistically, PbEE delivered abundant miR-423-3p to CMs, which subsequently enhanced glycolytic flux *via* the miR-423-3p/ZBTB7A/PKM2 axis, ultimately promoting CM proliferation and suppressing apoptosis. Furthermore, we encapsulated PbEE into GelMA-based MN patches to establish a stable EV delivery system. Compared with direct intramyocardial injection, the PbEE-loaded MN patches achieved sustained EV release and exerted superior therapeutic effects on MI.

6. Limitations of the study

First, EVs are complex natural delivery systems that harbor diverse biomolecular cargoes, including proteins, lipids, and nucleic acids, which collectively contribute to EV-mediated intercellular communication and biological functions[10]. Although our study identified miR-423-3p as a critical and indispensable effector underlying the enhanced cardioprotective effects of PbEE, the potential contributory or synergistic roles of other EV components cannot be completely ruled out. Further studies are warranted to clarify the potential synergistic effects of other EV-derived biomolecules. Furthermore, the clinical feasibility of the GelMA MN patch strategy requires careful consideration. While we have demonstrated effective delivery and sustained release of PbEE in mice without acute adverse effects, translating MN-based penetration into human myocardium remains challenging. The continuous beating, thicker ventricular wall, and potential risks of perforation or arrhythmia in the human heart demand higher standards for implantation precision, mechanical safety, and biocompatibility. Moreover, as an invasive procedure, whether the microscale injury induced by MNs may trigger undesired outcomes under certain pathological conditions remains to be systematically and long-term evaluated in more clinically relevant large animal models. Future work should focus on optimizing MN design parameters, developing safer implantation and navigation techniques, and rigorously assessing long-term safety and efficacy in settings that better mimic human cardiac physiology and pathology.

Acknowledgments

We are grateful for the support from the National Natural Science Foundation of China (U25A20184 and 92468301 to Benzhi Cai,

cardiomyocytes in total cardiomyocytes) on Day 14 post-MI ($n = 6$). Scale bar, 20 μm. (E) Representative immunofluorescence images and quantification of $Ki67^+$, $pH3^+$, and Aurora B^+ cardiomyocytes in the border zone at Day 14 post-MI ($n = 6$). White arrows: positive cardiomyocytes; boxed regions: magnified views. Scale bars: 20 μm (main image) and 10 μm (magnification). (F) Representative TUNEL staining (red) and quantification of apoptotic cardiomyocytes in the infarct border zone on Day 7 post-MI ($n = 6$). Scale bars: 20 μm (main image) and 10 μm (magnification). (G) CD31 immunofluorescence (green) and capillary density quantification in the border zone on Day 28 post-MI ($n = 6$). Scale bar, 20 μm. (H, I) Western blot analysis of ZBTB7A and PKM2 protein levels in the infarct border zone ($n = 4$). (J) Representative H&E staining of mouse hearts treated with PbEE@MN for 6, 8, and 10 weeks. Scale, 50 μm. (K) qRT-PCR analysis of *Desmin*, *Vimentin*, and *Calb2* in the hearts of MI mice treated with PbEE@MN ($n = 4$). (L) Residual EVs were harvested at Day 14 post-MN release and quantified using nanoparticle tracking analysis (NTA) ($n = 4$). (M) Representative H&E staining of major organs (liver, spleen, kidney, brain, lung) on Day 28 post-treatment ($n = 3$). Scale bar, 200 μm. Data are shown as mean ± SEM. $^*P < 0.05$, $^{**}P < 0.01$, $^{***}P < 0.001$.

82300302 to Yining Liu), the Key Project of Natural Science Foundation of Heilongjiang Province (ZL2024H017 to Benzhi Cai, China), and the China Postdoctoral Science Foundation (2023M730890 to Yining Liu). We thank BioRender.com for providing graphical illustration support in this study.

Author contributions

Yining Liu: Conceptualization, Data curation, Investigation, Visualization; Writing - original draft, Funding acquisition. Sijia Li: Data curation, Investigation, Methodology, Formal analysis. Ao Cai: Data curation, Investigation, Methodology. Wei Li: Investigation, Methodology, Formal analysis. Wanyu Zhang: Investigation, Methodology. Tianlong Li: Methodology, Software, Supervision. Manjie Zhang: Methodology, Visualization. Chenlu Liu: Investigation, Methodology. Wenya Ma: Writing - review & editing, Supervision. Yuqing Lin: Methodology, Investigation. Hanjing Li: Data curation. Xinlu Gao: Data curation, Formal analysis. Zhongyu Ren: Methodology, Validation. Hang Yu: Validation, Visualization. Haoyu Ji: Formal analysis, Data curation. Xiuxiu Wang: Investigation, Methodology. Yang Yu: Data curation, Formal analysis. Xu Liu: Investigation. Yifu Shen: Investigation. Ye Tian: Supervision. Faqian Li: Supervision. Zhenwei Pan: Conceptualization, Supervision, Writing - review & editing. Baofeng Yang: Conceptualization, Supervision, Project administration. Benzhi Cai: Conceptualization; Funding acquisition; Supervision; Writing - review & editing. Supervision.

Conflicts of interest

The authors declare no conflicts of interest.

Appendix A. Supporting information

Supporting information to this article can be found online at https://doi.org/10.1016/j.apsb.2026.04.015.

References

1. Tsao CW, Aday AW, Almarzooq ZI, Anderson CAM, Arora P, Avery CL, et al. Heart disease and stroke statistics-2023 update: a report from the American heart association. *Circulation* 2023;**147**: e93−621.
2. Frantz S, Hundertmark MJ, Schulz-Menger J, Bengel FM, Bauersachs J. Left ventricular remodelling post-myocardial infarction: pathophysiology, imaging, and novel therapies. *Eur Heart J* 2022;**43**: 2549−61.
3. Tang L, Qiu H, Xu B, Su Y, Nyarige V, Li P, et al. Microparticle mediated delivery of apelin improves heart function in post myocardial infarction mice. *Circ Res* 2024;**135**:777−98.
4. Fanaroff AC, Faggioni M. Managing myocardial infarction in the age of multimorbidity. *J Am Coll Cardiol* 2023;**82**:982−4.
5. Montague EC, Ozcan B, Sefton E, Wulkan F, Alibhai FJ, Laflamme MA. Human pluripotent stem cell-based cardiac repair: lessons learned and challenges ahead. *Adv Drug Deliv Rev* 2025;**222**: 115594.
6. Ilic D, Ogilvie C. Concise review: human embryonic stem cells—what have we done? What are we doing? Where are we going?. *Stem Cell* 2017;**35**:17−25.
7. Yamanaka S. Pluripotent stem cell-based cell therapy-promise and challenges. *Cell Stem Cell* 2020;**27**:523−31.
8. Menasche P. Cell therapy trials for heart regeneration—lessons learned and future directions. *Nat Rev Cardiol* 2018;**15**:659−71.
9. Iannotta D, A A, Kijas AW, Rowan AE, Wolfram J. Entry and exit of extracellular vesicles to and from the blood circulation. *Nat Nanotechnol* 2024;**19**:13−20.
10. Xu G, Jin J, Fu Z, Wang G, Lei X, Xu J, et al. Extracellular vesicle-based drug overview: research landscape, quality control and nonclinical evaluation strategies. *Signal Transduct Targeted Ther* 2025;**10**:255.
11. Tan F, Li X, Wang Z, Li J, Shahzad K, Zheng J. Clinical applications of stem cell-derived exosomes. *Signal Transduct Targeted Ther* 2024; **9**:17.
12. Tenchov R, Sasso JM, Wang X, Liaw WS, Chen CA, Zhou QA. Exosomes horizontal line nature's lipid nanoparticles, a rising star in drug delivery and diagnostics. *ACS Nano* 2022;**16**:17802−46.
13. Yu L, Wen H, Liu C, Wang C, Yu H, Zhang K, et al. Embryonic stem cell-derived extracellular vesicles rejuvenate senescent cells and antagonize aging in mice. *Bioact Mater* 2023;**29**:85−97.
14. Zhu Q, Ling X, Yang Y, Zhang J, Li Q, Niu X, et al. Embryonic stem cells-derived exosomes endowed with targeting properties as chemotherapeutics delivery vehicles for glioblastoma therapy. *Adv Sci (Weinh)* 2019;**6**:1801899.
15. Khan M, Nickoloff E, Abramova T, Johnson J, Verma SK, Krishnamurthy P, et al. Embryonic stem cell-derived exosomes promote endogenous repair mechanisms and enhance cardiac function following myocardial infarction. *Circ Res* 2015;**117**:52−64.
16. Kimiz-Gebologlu I, Oncel SS. Exosomes: large-scale production, isolation, drug loading efficiency, and biodistribution and uptake. *J Control Release* 2022;**347**:533−43.
17. Yao J, Huang K, Zhu D, Chen T, Jiang Y, Zhang J, et al. A minimally invasive exosome spray repairs heart after myocardial infarction. *ACS Nano* 2021;**15**:11099−111.
18. Li J, Sun S, Zhu D, Mei X, Lyu Y, Huang K, et al. Inhalable stem cell exosomes promote heart repair after myocardial infarction. *Circulation* 2024;**150**:710−23.
19. Erwin N, Serafim MF, He M. Enhancing the cellular production of extracellular vesicles for developing therapeutic applications. *Pharm Res* 2023;**40**:833−53.
20. Maghfour J, Ozog DM, Mineroff J, Jagdeo J, Kohli I, Lim HW. Photobiomodulation CME part I: overview and mechanism of action. *J Am Acad Dermatol* 2024;**91**:793−802.
21. Selestin Raja I, Kim C, Oh N, Park JH, Hong SW, Kang MS, et al. Tailoring photobiomodulation to enhance tissue regeneration. *Biomaterials* 2024;**309**:122623.
22. Gao X, Li H, Zhang W, Wang X, Sun H, Cao Y, et al. Photobiomodulation drives mir-136-5p expression to promote injury repair after myocardial infarction. *Int J Biol Sci* 2022;**18**:2980−93.
23. Lee SY, Jeon S, Kwon YW, Kwon M, Kang MS, Seong KY, et al. Combinatorial wound healing therapy using adhesive nanofibrous membrane equipped with wearable LED patches for photobiomodulation. *Sci Adv* 2022;**8**. eabn1646.
24. Sourvanos D, Lander B, Sarmiento H, Carroll J, Hall RD, Zhu TC, et al. Photobiomodulation in dental extraction therapy: postsurgical pain reduction and wound healing. *J Am Dent Assoc* 2023;**154**: 567−79.
25. Da Silva D, van Rensburg MJ, Crous A, Abrahamse H. Photobiomodulation: a novel approach to promote trans-differentiation of adipose-derived stem cells into neuronal-like cells. *Neural Regen Res* 2025;**20**:598−608.
26. Shi Z, Li S, Chen W, Yan H. The effect of blue and green light on human umbilical cord mesenchymal stem cells for promoting proliferation and wound healing. *Sci Rep* 2025;**15**:14787.
27. Zeng Y, Wang C, Lei J, Jiang X, Lei K, Jin Y, et al. Spatiotemporally responsive cascade bilayer microneedles integrating local glucose depletion and sustained nitric oxide release for accelerated diabetic wound healing. *Acta Pharm Sin B* 2024;**14**:5037−52.
28. Jin Y, Liu S, Wang X, Wang C, Ruan Q, Li W. Multifunctional microneedle patches loaded with engineered nitric oxide-releasing nanocarriers for targeted and synergistic chronic wound therapy. *Adv Mater* 2025;**37**:e2413108.

29. Jiang P, Zeng Y, Zhang W, Lei J, Jiang X, Li W. Three-in-one bilayer microneedle patch for ultrasound-activated antibacterial therapy and immune modulation in wound healing. *J Control Release* 2025;**388**: 114375.
30. Zucker I, Beery AK. Males still dominate animal studies. *Nature* 2010;**465**:690.
31. Lindsey ML, Bolli R, Canty JM Jr, Du XJ, Frangogiannis NG, Frantz S, et al. Guidelines for experimental models of myocardial ischemia and infarction. *Am J Physiol Heart Circ Physiol* 2018;**314**: H812−38.
32. Ravi V, Jain A, Taneja A, Chatterjee K, Sundaresan NR. Isolation and culture of neonatal murine primary cardiomyocytes. *Curr Protoc* 2021;**1**:e196.
33. Li D, Liu Y, Li C, Zhou Z, Gao K, Bao H, et al. Spexin diminishes atrial fibrillation vulnerability by acting on galanin receptor 2. *Circulation* 2024;**150**:111−27.
34. Han Z, Xu Z, Yu Y, Cao Y, Bao Z, Gao X, et al. ALKBH5-mediated m^6A mRNA methylation governs human embryonic stem cell cardiac commitment. *Mol Ther Nucleic Acids* 2021;**26**:22−33.
35. Wu X, Reboll MR, Korf-Klingebiel M, Wollert KC. Angiogenesis after acute myocardial infarction. *Cardiovasc Res* 2021;**117**:1257−73.
36. Li Y, Chen X, Jin R, Chen L, Dang M, Cao H, et al. Injectable hydrogel with MSNs/microRNA-21-5p delivery enables both immunomodification and enhanced angiogenesis for myocardial infarction therapy in pigs. *Sci Adv* 2021;**7**. eabd6740.
37. Kong P, Zhu X, Geng Q, Xia L, Sun X, Chen Y, et al. The microRNA-423-3p−Bim axis promotes cancer progression and activates oncogenic autophagy in gastric cancer. *Mol Ther* 2017;**25**:1027−37.
38. Liu Z, Cui Y. Bim's effect on the expression of miR-423-3p in promoting primary hepatic cancer (PHC) and role of miR-423-3p in PHC proliferation and invasion. *Biochem Genet* 2021;**59**:1247−59.
39. Da Silva D, Crous A, Abrahamse H. Enhancing osteogenic differentiation in adipose-derived mesenchymal stem cells with near infra-red and green photobiomodulation. *Regen Ther* 2023;**24**:602−16.
40. Serrage H, Heiskanen V, Palin WM, Cooper PR, Milward MR, Hadis M, et al. Under the spotlight: mechanisms of photobiomodulation concentrating on blue and green light. *Photochem Photobiol Sci* 2019;**18**:1877−909.
41. Ma W, Tian Y, Shi L, Liang J, Ouyang Q, Li J, et al. *N*-Acetyltransferase 10 represses uqcr11 and uqcrb independently of ac4C modification to promote heart regeneration. *Nat Commun* 2024;**15**: 2137.
42. Fukuda R, Marin-Juez R, El-Sammak H, Beisaw A, Ramadass R, Kuenne C, et al. Stimulation of glycolysis promotes cardiomyocyte proliferation after injury in adult zebrafish. *EMBO Rep* 2020;**21**:e49752.
43. Han D, Chen S, Han W, Gao S, Owiredu JN, Li M, et al. ZBTB7A mediates the transcriptional repression activity of the androgen receptor in prostate cancer. *Cancer Res* 2019;**79**:5260−71.
44. Redondo Monte E, Kerbs P, Greif PA. ZBTB7A links tumor metabolism to myeloid differentiation. *Exp Hematol* 2020;**87**. 20-4.e1.
45. Bei Y, Zhu Y, Zhou J, Ai S, Yao J, Yin M, et al. Inhibition of Hmbox1 promotes cardiomyocyte survival and glucose metabolism through Gck activation in ischemia/reperfusion injury. *Circulation* 2024;**150**:848−66.
46. Zhao Y, Pan Y, Chen M, Tan Y, Chang X, Li H, et al. PKM2 interacts with and phosphorylates PHB2 to sustain mitochondrial quality control against septic cerebral-cardiac injury. *Int J Med Sci* 2024;**21**: 633−43.
47. Qi W, Keenan HA, Li Q, Ishikado A, Kannt A, Sadowski T, et al. Pyruvate kinase M2 activation may protect against the progression of diabetic glomerular pathology and mitochondrial dysfunction. *Nat Med* 2017;**23**:753−62.
48. Tang J, Wang J, Huang K, Ye Y, Su T, Qiao L, et al. Cardiac cell-integrated microneedle patch for treating myocardial infarction. *Sci Adv* 2018;**4**. eaat9365.
49. Gabisonia K, Prosdocimo G, Aquaro GD, Carlucci L, Zentilin L, Secco I, et al. MicroRNA therapy stimulates uncontrolled cardiac repair after myocardial infarction in pigs. *Nature* 2019;**569**:418−22.
50. Han C, Yang J, Sun J, Qin G. Extracellular vesicles in cardiovascular disease: biological functions and therapeutic implications. *Pharmacol Ther* 2022;**233**:108025.
51. Li G, Chen T, Dahlman J, Eniola-Adefeso L, Ghiran IC, Kurre P, et al. Current challenges and future directions for engineering extracellular vesicles for heart, lung, blood and sleep diseases. *J Extracell Vesicles* 2023;**12**:e12305.
52. Yadav A, Gupta A. Noninvasive red and near-infrared wavelength-induced photobiomodulation: promoting impaired cutaneous wound healing. *Photodermatol Photoimmunol Photomed* 2017;**33**:4−13.
53. Yang Y, Yang R, Deng F, Yang L, Yang G, Liu Y, et al. Immunoactivation by cutaneous blue light irradiation inhibits remote tumor growth and metastasis. *ACS Pharmacol Transl Sci* 2024;**7**:1055−68.
54. Luo H, Li X, Li T, Zhao L, He J, Zha L, et al. MicroRNA-423-3p exosomes derived from cardiac fibroblasts mediates the cardioprotective effects of ischaemic post-conditioning. *Cardiovasc Res* 2019;**115**:1189−204.
55. Magadum A, Singh N, Kurian AA, Munir I, Mehmood T, Brown K, et al. Pkm2 regulates cardiomyocyte cell cycle and promotes cardiac regeneration. *Circulation* 2020;**141**:1249−65.
56. Rihan M, Zangi L, Magadum A. Pyruvate kinase M2 role in cardiovascular repair. *Cells* 2025;**14**:1623.
57. Gao J, Zhao Y, Li T, Gan X, Yu H. The role of PKM2 in the regulation of mitochondrial function: focus on mitochondrial metabolism, oxidative stress, dynamic, and apoptosis. PKM2 in mitochondrial function. *Oxid Med Cell Longev* 2022;**2022**:7702681.
58. Wu X, Liu L, Zheng Q, Hao H, Ye H, Li P, et al. Protocatechuic aldehyde protects cardiomycoytes against ischemic injury *via* regulation of nuclear pyruvate kinase M2. *Acta Pharm Sin B* 2021;**11**: 3553−66.
59. Chen S, Yao H, Lou Y, Wang H, Xie B, Wu J, et al. Pharmacological upregulation of macrophage-derived itaconic acid by pubescenoside C attenuated myocardial ischemia−reperfusion injury. *J Adv Res* 2025; **74**:571−87.
60. Fathi-Karkan S, Heidarzadeh M, Narmi MT, Mardi N, Amini H, Saghati S, et al. Exosome-loaded microneedle patches: promising factor delivery route. *Int J Biol Macromol* 2023;**243**:125232.
61. Zhang X, Hasani-Sadrabadi MM, Zarubova J, Dashtimighadam E, Haghniaz R, Khademhosseini A, et al. Immunomodulatory microneedle patch for periodontal tissue regeneration. *Matter* 2022;**5**:666−82.
62. Zhu J, Zhou X, Kim HJ, Qu M, Jiang X, Lee K, et al. Gelatin methacryloyl microneedle patches for minimally invasive extraction of skin interstitial fluid. *Small* 2020;**16**:e1905910.
63. Chen H, Fan L, Peng N, Yin Y, Mu D, Wang J, et al. Galunisertib-loaded gelatin methacryloyl hydrogel microneedle patch for cardiac repair after myocardial infarction. *ACS Appl Mater Interfaces* 2022; **14**:40491−500.